Synthesis and properties of N-methylimidazole solvates of vanadium(II), chromium(II) and iron(II) phthalocyanines. Strong NIR absorption in VII(MeIm)2(Pc2−)

AUTHOR(S):

Konarev, Dmitri V.; Kuz`min, Alexey V.; Nakano, Yoshiaki; Khasanov, Salavat S.; Otsuka, Akihiro; Yamochi, Hideki; Kitagawa, Hiroshi; Lyubovskaya, Rimma N.

CITATION:

Konarev, Dmitri V. ...[et al]. Synthesis and properties of N-methylimidazole solvates of vanadium(II), chromium(II) and iron(II) phthalocyanines. Strong NIR absorption in VII(MeIm)2(Pc2−). Dalton Transactions 2018, 47(13): 4661-4671

ISSUE DATE:

2018-02-21

URL:

http://hdl.handle.net/2433/230322

Journal Name

PAPER

Received 00th January 20xx,

Accepted 00th January 20xx

DOI: 10.1039/x0xx00000x

www.rsc.org/

Synthesis and properties of *N*-methylimidazole solvates of vanadium(II), chromium(II) and iron(II) phthalocyanines. Strong NIR absorption in $V^{II}(MeIm)_2(Pc^{2-})$.

Dmitri V. Konarev,*[a] Alexey V. Kuzmin,[b] Yoshiaki Nakano,[c] Salavat S. Khasanov,[b] Akihiro Otsuka,[c, d] Hideki Yamochi,[c, d] Hiroshi Kitagawa,[c] Rimma N. Lyubovskaya[a]

N-methylimidazole (MeIm) solvates of vanadium(II), chromium(II) and iron(II) phthalocyanines: $[V^{II}(MeIm)_2(Pc^{2-})]^0 \cdot MeIm$ (**1**) and $[M^{II}(MeIm)_2(Pc^{2-})]^0 \cdot 2C_6H_4Cl_2$ (M = V (**2**), Cr (**3**), and Fe (**4**)) have been obtained and studied in a crystalline form. It has been shown that central metal atoms have +2 oxidation state in **1**-**4** and dianionic Pc^{2-} macrocycles are formed. Optical spectra of **1**–**3** (V^{II}, Cr^{II}) are different from that of **4** (Fe^{II}) due to the appearance of intense absorption bands in the NIR range at 1187 nm for **1** and **2** and 1178 nm for **3** and manifestation of multiple bands in the visible range. Absorption in the NIR range is explained by unusually small HOMO−LUMO gaps for MeIm solvated $Cr^{II}Pc$ and $V^{II}Pc$. Essential diradicaloid character of the Pc macrocycles in $[Cr^{II}(MeIm)_2(Pc^{2-})]^0$, in which α- and β-orbitals are distributed in different regions of the macrocycle has also been shown. In this case, the diradicaloid character is comparable to that of aromatic hydrocarbon heptacene. Magnetic properties of **1**–**3** are defined by metal atoms with $S = 3/2$ spin state for V^{II} and $S = 1$ for Cr^{II}. Compounds **1**–**3** manifest broad isotropic EPR signals at 4.2 K with g = 2.0188 and linewidth (ΔH) of 81.8 mT for **1** (V^{II}), g = 1.8300 and linewidth ΔH = 161.0 mT for **2** (V^{II}), and g = 2.0534 and ΔH = 60.27 mT for **3** (Cr^{II}). These signals shifted to smaller g-factors with the temperature increase. Integral intensity of narrow EPR signals from $Pc^{\bullet 3-}$ does not exceed 0.1% from those of broad signals in **1**–**3**. Complex **4** is EPR silent due to the presence of diamagnetic Fe^{II} and Pc^{2-}.

Introduction

Metal phthalocyanines can possess promising optical, conducting and magnetic properties.[1–7] For example, some phthalocyanine derivatives are used as sensors and materials for optical and photoelectronic devices.[1,2] Conducting compounds can be obtained by oxidation of metal-free and metal-containing phthalocyanines.[3–5] Oxidation of manganese(II) macroheterocycles or reduction of iron(II) phthalocyanine yields compounds with ferrimagnetic ordering of spins.[6,7]

Neutral metal phthalocyanines containing paramagnetic species the unpaired electron of which can participate in magnetic ordering of spins or conductivity attract special interest. Spin can be delocalized over phthalocyanine macrocycle or central metal atom. For example, neutral metal phthalocyanine compounds which contain phthalocyanine radical trianions or tetraanions are known: $M^{III}L_2(Pc^{\bullet 3-})$, (M = Al, Ga, L = THF, *N*-methylimidazole),[8,9] $Ge^{IV}(Pc^{4-})$,[10] $Zr^{IV}(Pc^{4-})$[11] and $Sn^{IV}Ph(Pc^{\bullet 3-})$[12]. Negative charge of the Pc macrocycles in these compounds is compensated by positive charge of a central metal atom. Metal centered reduction can also be used to obtain compounds with unusual oxidation state of metal atoms. Besides known pyridine solvates of iron(II), manganese(II) and cobalt(II) phthalocyanines of the $[M^{II}(Py)_2(Pc^{2-})]$ composition,[13, 14] compounds of solvated chromium(II) phthalocyanine are known, $[Cr^{II}(THF)_2(Pc^{2-})]^0$ and $[Cr^{II}(Py)_2(Pc^{2-})]^0$ [15, 16]. However, vanadium(II) phthalocyanine and its solvates as well as crystal structures of *N*-methylimidazole solvates of phthalocyanines of transition metals have not been studied so far.

In this work series of *N*-methylimidazole solvates of vanadium(II), chromium(II) and iron(II) phthalocyanines were obtained in a crystalline form: $[V^{II}(MeIm)_2(Pc^{2-})]^0 \cdot MeIm$ (**1**) and $[M^{II}(MeIm)_2(Pc^{2-})]^0 \cdot 2C_6H_4Cl_2$ (M = V (**2**), Cr (**3**), and Fe (**4**)) and their molecular structure, optical and magnetic properties were analyzed. Optical properties of $[Fe^{II}(MeIm)_2(Pc^{2-})]^0$ are typical for solvated metal(II) phthalocyanines.[13, 14] However, optical properties of $[Cr^{II}(MeIm)_2(Pc^{2-})]^0$ and $[V^{II}(MeIm)_2(Pc^{2-})]^0$ are different from those of **4** due to strong absorption in the NIR range and multiple bands in the visible

[a]Institute of Problems of Chemical Physics RAS, Chernogolovka, Moscow region, 142432 Russia, E-mail: konarev3@yandex.ru
[b]*Institute of Solid State Physics RAS, Chernogolovka, Moscow region, 142432 Russia;*
[c]*Division of Chemistry, Graduate School of Science, Kyoto University, Sakyo-ku, Kyoto 606-8502, Japan;*
[d]*Research Center for Low Temperature and Materials Sciences, Kyoto University, Sakyo-ku, Kyoto 606-8501, Japan*
Electronic Supplementary Information (ESI) available: The IR spectra of starting compounds and **1**-**4**, crystal structure of **1**, magnetic data of **1**-**3**, and the results of DFT and TD-DFT calculations. See DOI: 10.1039/x0xx00000x

range. To understand these features we carried out DFT calculations for solvates of vanadium(II) and chromium(II) phthalocyanines. Essential diradicaloid nature of the Pc macrocycles in $[Cr^{II}(MeIm)_2(Pc^{2-})]^0$ was found. This new peculiarity of the Pc macrocycles is very rare for macroheterocyclic compounds and was previously found only for nickel(II) and copper(II) corroles,[17] oxidized doubly linked corrole dimer and its zinc(II) complex[18].

Results and discussion

a. Synthesis.

Vanadyl phthalocyanine ($V^{IV}OPc$) can be reduced in *o*-dichlorobenzene by sodium fluorenone ketyl even in the presence of MeIm to form deep blue solution containing the $[V^{IV}O(Pc^{\bullet 3-})]^{\bullet -}$ radical anions. However, when reduction of $V^{IV}OPc$ is carried out in the presence of two equivalents of chromium(II) chloride and samarium(II) iodide ($Cr^{II}Cl_2$ or $Sm^{II}I_2$), the color of the solution changes from deep blue to brown-violet indicating the formation of a new product. Slow mixing of this brown-violet solution with *n*-hexane allows the isolation of good quality single crystals which according to the X-ray diffraction data have the $[V^{II}(MeIm)_2(Pc^{2-})]^0 \cdot MeIm$ (**1**, for SmI_2) and $[V^{II}(MeIm)_2(Pc^{2-})]^0 \cdot 2C_6H_4Cl_2$ (**2**, for $CrCl_2$) compositions. Therefore, reduction of V^{IV} to V^{II} is realized by sodium fluorenone ketyl and the $Cr^{II}Cl_2$ or $Sm^{II}I_2$ salts abstract oxygen ligand from vanadium. Interestingly that this reaction is completely reversible, and when we filtered the brown-violet solution and added one more equivalent of sodium fluorenone ketyl with cryptand[2.2.2.], deep blue solution was restored immediately showing the formation of $[V^{IV}O(Pc^{\bullet 3-})]^{\bullet -}$ due to that vanadium atoms abstract oxygen from fluorenone ketyl. Known salt $[cryptand[2.2.2](Na^+)][V^{IV}O(Pc^{\bullet 3-})]^{\bullet -} \cdot C_6H_4Cl_2$ [19] was obtained in this case. Finally we found that reduction of $[V^{IV}O(Pc^{2-})]^0$ to $[V^{II}(MeIm)_2(Pc^{2-})]^0$ can be performed without sodium fluorenone ketyl. The reaction of $[V^{IV}O(Pc^{2-})]^0$ with two equivalents of $Cr^{II}Cl_2$ or $Sm^{II}I_2$ in the presence of 0.2 mL of MeIm at 80°C proceeds at essentially lower rate and can be finished during 24 hours. $Cr^{II}Cl_2$ and $Sm^{II}I_2$ are strong reductants (E_{redox} of Cr^{II}/Cr^{III} is -0.42 V and E_{redox} of Sm^{II}/Sm^{III} is -1.3 V *vs* SCE)[20] which potentially can reduce metal phthalocyanines. They are insoluble in pure *o*-dichlorobenzene. Addition of *N*-methylimidazole allows one to dissolve these salts as *N*-methylimidazole solvates and use them as reductants.

Similar reactions were carried out with $Ti^{IV}OPc$ and $Cr^{III}ClPc$ with the formation of brown-violet and green-blue solutions but only crystals of $[Cr^{II}(MeIm)_2(Pc^{2-})]^0 \cdot 2C_6H_4Cl_2$ (**3**) suitable for X-ray diffraction study were obtained. We also found that only metal phthalocyanines with strongly bound metals like V and Ti can be used in these reactions. The use of $Cr^{II}Cl_2$ as reductant for phthalocyanines with metals weaker bonded to phthalocyanines like $Sn^{IV}Cl_2$ and $In^{III}Cl$ provides the formation of $[Cr^{II}(MeIm)_2(Pc^{2-})]^0 \cdot 2C_6H_4Cl_2$ (**3**) only (crystals obtained in these reactions have the same crystal structures and spectra as **3**). Therefore, chromium(II) substitutes $Sn^{IV}Cl_2$ and $In^{III}Cl$ in phthalocyanines instead of reduction.

Data for $[Fe^{II}(MeIm)_2(Pc^{2-})]^0 \cdot 2C_6H_4Cl_2$ (**4**) were added to compare its properties with those of vanadium(II) and chromium(II) solvates. Crystals of this solvate can be obtained by dissolution of $Fe^{II}Pc$ in the presence of MeIm.

b. Crystal structures.

Crystals of **1**-**4** were studied by X-ray diffraction at 130-150 K. Geometric parameters of the coordination $[M^{II}(MeIm)_2(Pc^{2-})]^0$ units are listed in Table 1 and their molecular structures are shown in Fig. 1 for $[V^{II}(MeIm)_2(Pc^{2-})]^0$ in **1** as an example. The MeIm ligands coordinate to the metal centers from both sides of the macrocycles and metal atoms have slightly distorted octahedral environment in **1**–**4**. Despite the deformation metal atoms are positioned exactly in the 24-atom Pc planes. Vanadium atoms in **1** and **2** form the longest V^{II}–N(Pc) and V^{II}–N(MeIm) bonds of 2.00 and 2.15 Å length, respectively. The length of these bonds is shortened to 1.98 and 2.09 Å for chromium(II) phthalocyanine in **3**, respectively, and the shortest Fe^{II}–N(Pc) and Fe^{II}–N(MeIm) bonds are observed for iron(II) phthalocyanine in **4** – 1.93 and 1.96-2.02 Å, respectively. It is interesting that there are two orientations of the coordinated MeIm ligand in $[Fe^{II}(MeIm)_2(Pc^{2-})]^0$. These orientations are related by the rotation of the MeIm ligand about the Fe^{II}–N(MeIm) bond by 174.23°. Different rotation angle provides different conditions for the coordination of MeIm to Fe^{II} and the length of the Fe^{II}–N(MeIm) bonds changes from 1.964(14) Å for minor orientation of MeIm to 2.018 Å for major orientation of MeIm.

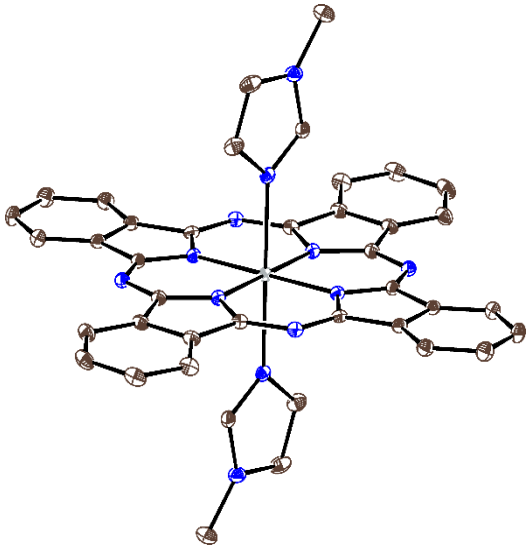

Fig. 1. Molecular structure of the coordination $[V^{II}(MeIm)_2(Pc^{2-})]^0$ unit in **1**. The coordination $[Cr^{II}(MeIm)_2(Pc^{2-})]^0$ and $[Fe^{II}(MeIm)_2(Pc^{2-})]^0$ units in **3** and **4**, respectively have similar geometry. Ellipsoid probability is 25%.

Geometry of the Pc macrocycle is sensitive to its charged state since distortions are induced at the transition from stable 18 π-electron system of Pc^{2-} to less stable 19 π-electron system of $Pc^{\bullet 3-}$ and 20 π-electron system of Pc^{4-}.[10, 16, 21] Indeed, the alternation of the C–N(imine) bonds was found[9] in

Table 1. Geometric parameters of pristine metal phthalocyanines and their MeIm solvates.

Compound	Average bond length in macrocycle, Å				Average M-N(Pc) bond, Å	The M-N(MeIm) bond, Å
	C–N (pyr)	C–N (imine) short	C–N (imine) long	C–N (imine) difference		
$Al^{III}(MeIm)_2(Pc^{\bullet 3-})$ ·MeIm [9] 2 units	1.385(3) 1.383(3)	1.320(3) 1.319(3)	1.347(3) 1.342(3)	0.027 0.023	1.954(2) 1.958(2)	2.052(2) 2.059(2)
$Ga^{III}(MeIm)_2(Pc^{\bullet 3-})$·$2C_6H_4Cl_2$ [9] 1 unit	1.385(1)	1.317(1)	1.358(1)	0.031	1.987(1)	2.161(1)
$V^{IV}O(Pc^{2-})$ [22]	1.387(4)	1.334(4)		0	2.044(4)	-
$[V^{II}(MeIm)_2(Pc^{2-})]$·MeIm (**1**) 2 units	1.384(2) 1.382(2)	1.337(2) 1.335(2)	1.340(2) 1.339(2)	0.003 0.004	1.998(1) 2.000(1)	2.149(1) 2.142(1)
$[V^{II}(MeIm)_2(Pc^{2-})]$·$2C_6H_4Cl_2$ (**2**) 1 unit	1.380(1)	1.336(1)	1.337(1)	0.001	1.998(1)	2.151(1)
$[Cr^{II}(MeIm)_2(Pc^{2-})]$·$2C_6H_4Cl_2$ (**3**) 1 unit	1.381(3)	1.314(3)	1.348(3)	0.034	1.976(2)	2.086(2)
$[Fe^{II}(MeIm)_2(Pc^{2-})]$·$2C_6H_4Cl_2$ (**4**) 1 unit	1.376(4)	1.323(3)	1.334(3)	0.011	1.935(2)	2.018(3) 91% 1.964(14) 9%

previously studied $[M^{III}(MeIm)_2(Pc^{\bullet 3-})]^{\bullet}$ radicals which according to the optical and magnetic data contain radical trianionic $Pc^{\bullet 3-}$ macrocycles. The difference between average short and long C–N(imine) bonds of 0.023-0.031 Å (Table 1) essentially exceeds of the standard deviation (3σ = 0.009 Å). It is seen that for $[V^{II}(MeIm)_2(Pc^{2-})]$ the difference between short and long C–N(imine) bonds of 0.001–0.004 Å is close to zero. This difference is larger for $[Fe^{II}(MeIm)_2(Pc^{2-})]$ (0.011 Å) but it is still close to the 3σ value. Only in the case of $[Cr^{II}(MeIm)_2(Pc^{2-})]$, X-ray diffraction data show the alternation of the C–N(imine) bonds (the difference between short and long bonds is 0.034 Å) and in this case an excess negative charge on the Pc macrocycle can be supposed.

In spite of similar geometry of the $[M(MeIm)_2Pc]$ units (M = Al^{III}, Ga^{III}, V^{II}, Cr^{II}, and Fe^{II}), different packing modes of these units are observed in the obtained compounds. Insertion of MeIm provides the formation of isostructural $M(MeIm)_2Pc$·MeIm (M = Al^{III} and V^{II} (**1**)) compounds with two halves of crystallographically independent $M(MeIm)_2Pc$ units. Packing of $M(MeIm)_2Pc$ in **1** is shown in Fig. S5. They form chains along the *b* axis with long distances between the Pc macrocycles defined by size of the coordinated MeIm ligand. Neighboring chains are directed in perpendicular directions and the angle between the Pc planes from the neighboring chains is close to 90°. There is no π-π interaction between the Pc macrocycles in such packing mode. Complex $[V^{II}(MeIm)_2(Pc^{2-})]$·$2C_6H_4Cl_2$ (**2**) has different packing mode. The main structural motif is a one-dimensional π-stacking chain directed along the *b* axis with several side-by-side short van der Waals contacts between the Pc macrocycles shown by green dashed lines in Fig. 2a. The Pc macrocycles have different incline in the neighboring chains forming an angle between the Pc macrocycles of 51.2°. Other compounds $[M(MeIm)_2Pc]$·$2C_6H_4Cl_2$ (M = Cr^{II} (**3**), Fe^{II} (**4**), and Ga^{III}) are isostructural and also contain one-dimensional chains from the Pc macrocycles. However, all macrocycles are parallel to each other (Fig. 3b). Large vacancies are formed at such packing shown by green ovals in Fig. 2b. These vacancies are occupied by strongly disordered solvent $C_6H_4Cl_2$ molecules.

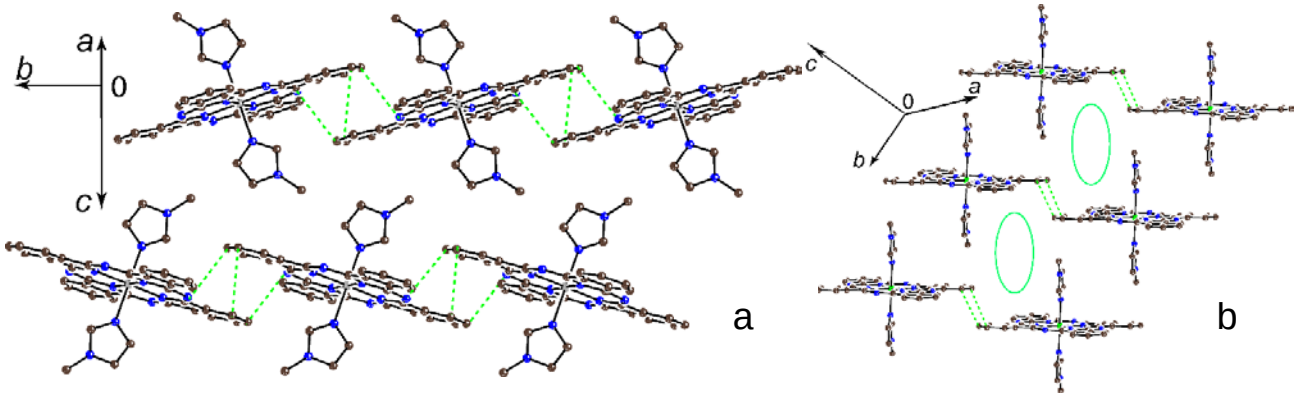

Fig. 2. View on the crystal structures of: (a) $[V^{II}(MeIm)_2(Pc^{2-})]^0$·$2C_6H_4Cl_2$ (**2**), solvent molecules are not shown for clarity; (b) $[Cr^{II}(MeIm)_2(Pc^{2-})]^0$·$2C_6H_4Cl_2$ (**3**), channels occupied by disordered solvent $C_6H_4Cl_2$ molecules are shown by green ovals. Compound **4** is isostructural to **3**.

c. Optical properties.

Generally, metal phthalocyanines with dianionic Pc^{2-} ligand show similar spectra containing Soret and Q bands. The Q-band is manifested in the spectrum of $V^{IV}OPc$ as a broad band split into three lines with maxima at 657, 721 and 812 nm (Fig. 3a) whereas three bands are not well pronounced in the spectrum of pristine $Fe^{II}Pc$ and maximum of the Q-band is observed at about 670 nm (Fig. 3c). Soret bands are observed in the spectra of $V^{IV}OPc$ and $Fe^{II}Pc$ at 347 and 326 nm, respectively. Coordination of two imidazole ligands to iron(II) in $[Fe^{II}(MeIm)_2(Pc^{2-})]^0$ has a small effect on the spectrum of iron(II) phthalocyanine. Bands are narrowed but retain their position with the maximum at 670 nm (a weaker band is manifested at 610 nm) and the Soret band is positioned at 345 nm (Fig. 3c). Coordination provides the appearance of one new band in the spectrum of $[Fe^{II}(MeIm)_2(Pc^{2-})]^0$ at 429 nm (Fig. 3c). Such band is also observed at 414 nm in the spectrum of $[Fe^{II}(Py)_2(Pc^{2-})]^0$ in the complex with fullerene C_{60}.[23] Spectra of MeIm solvated vanadium(II) and chromium(II) phthalocyanines are strongly different from that of $[Fe^{II}(MeIm)_2(Pc^{2-})]^0$. First of all, $[V^{II}(MeIm)_2(Pc^{2-})]^0$ in both **1** and **2** shows very intense absorption bands in the NIR range with maxima 1187, 1090 and 1026 nm (Fig. 3a). As we show below, these bands are not associated with the radical $Pc^{\bullet 3-}$ trianions which appear at the macrocycle reduction. For example, in $M^{III}(MeIm)_2(Pc^{\bullet 3-})$ (M = Al^{III}, Ga^{III}) these bands are manifested at 994-999 nm.[9] For **1**–**3**, bands in the NIR range are associated with HOMO-LUMO transitions which have unusually low energy for vanadium(II) and chromium(II) phthalocyanines (according to the DFT calculations). Another interesting peculiarity is splitting of the Q-band into six bands at least, which spread over almost all visible range since these bands have maxima at 680, 617, 558, 514, 496, and 464 nm (Fig. 3a). All these bands are well reproduced in the spectra of both compounds **1** and **2**. The Soret band is manifested in the spectra of **1** and **2** as an intense single band with maximum at 347 nm, and its position coincides with that for pristine $V^{IV}OPc$. Chromium(II) phthalocyanine, $[Cr^{II}(MeIm)_2(Pc^{2-})]^0$, also manifests bands in the NIR range. However, the lowest energy bands at 1178 and 1006 nm become weaker in comparison with the spectra of **1** and **2** but a new intense band is observed at 841 nm (Fig. 3b) (the latter band is not observed in the spectrum of $[V^{II}(MeIm)_2(Pc^{2-})]^0$). The Q-band is also split in the spectrum of **3** into five bands manifested at 689, 631, 579, 534, and 491 nm (Fig. 3b). The Soret band shows two peaks in the spectrum of **3** with maxima at 392 and 330 nm. Thus, spectra of $[V^{II}(MeIm)_2(Pc^{2-})]^0$ and $[Cr^{II}(MeIm)_2(Pc^{2-})]^0$ are different from that of $[Fe^{II}(MeIm)_2(Pc^{2-})]^0$. To understand these differences we carried out DFT calculations presented below.

d. Magnetic properties.

Magnetic properties of pristine $Fe^{II}Pc$ and $Cr^{II}Pc$ as well as their pyridine solvates were studied previously.[14, 15, 24] It is shown that pristine metal(II) phthalocyanines have high spin state: S =1 for $Fe^{II}Pc$[24] and S = 2 for $Cr^{II}Pc$.[15] Coordination of pyridine ligands provides transition to the lower spin state: S = 0 for $[Fe^{II}(Py)_2(Pc^{2-})]$[14] and S = 1 for $[Cr^{II}(Py)_2(Pc^{2-})]$[15]. Magnetic properties of $V^{II}Pc$ and its solvates are unknown.

Magnetic properties of **1**–**3** were studied by SQUID and EPR techniques but those of **4** were studied by EPR. Effective magnetic moments of **1** and **2** are equal to 3.89 and 3.84 μ_B at 300 K (Figs. 4a and 4b), indicating S = 3/2 spin state for $V^{II}Pc$ solvated by MeIm (the calculated magnetic moment for the noninteracting S = 3/2 system is 3.87 μ_B at g = 2). This indicates that the coordination of MeIm provides the highest spin state of V^{II}. Effective magnetic moment for $[Cr^{II}(MeIm)_2(Pc^{2-})]\cdot 2C_6H_4Cl_2$ (**3**) is equal to 2.77 μ_B at 300 K (Fig. 4c), indicating intermediate S = 1 spin state for Cr^{II}. The calculated magnetic moment is 2.83 μ_B for the noninteracting S = 1 system at g = 2. Therefore, in the case of $Cr^{II}Pc$, the lowering of magnetic moment was observed at the coordination of two MeIm ligands in comparison with pristine $Cr^{II}Pc$ having S = 2 spin state. Similar behavior is observed at the coordination of two pyridine ligands to Cr^{II} (S = 1)[15]. Temperature dependencies of reciprocal molar magnetic susceptibility for **1**–**3** are shown in Fig. S6. These dependencies are linear allowing to Weiss temperature to be determined as −2 K for all three compounds. These data indicate that only weak antiferromagnetic coupling is realized between paramagnetic centers in **1**–**3** most probably due to the absence of effective π-π interactions between the Pc macrocycles and localization of spin density mainly on paramagnetic metal atoms positioned far from each other (all M···M distances are longer than 10 Å).

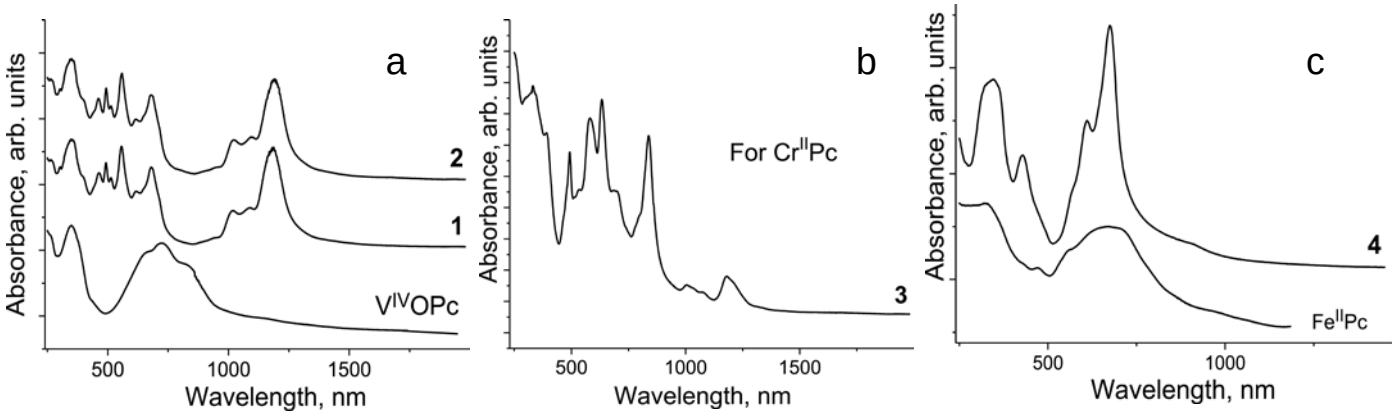

Fig. 3. Spectra of pristine compounds ($V^{IV}OPc$ and $Fe^{II}Pc$) and compounds **1**–**4** in the UV-visible-NIR range in KBr pellets prepared in anaerobic conditions.

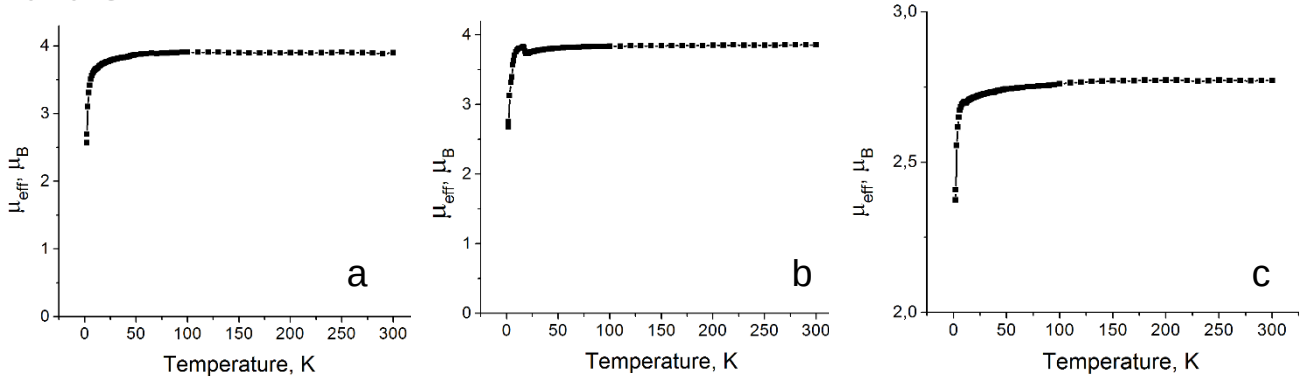

Fig. 4. Temperature dependencies of effective magnetic moments for polycrystalline compounds **1** (a); **2** (b) and **3** (c).

EPR spectra of **1**–**3** show broad signals in the whole studied temperature range of 4.2–293 K, which unambiguously can be attributed to paramagnetic metal atoms. Compound **1** shows a broad EPR signal at 293 K with g = 1.9889 and the linewidth (ΔH) of 54.2 mT attributed to V^{II} (Fig. 5a). This signal shifts to higher g-factors and broadens with the temperature decrease,

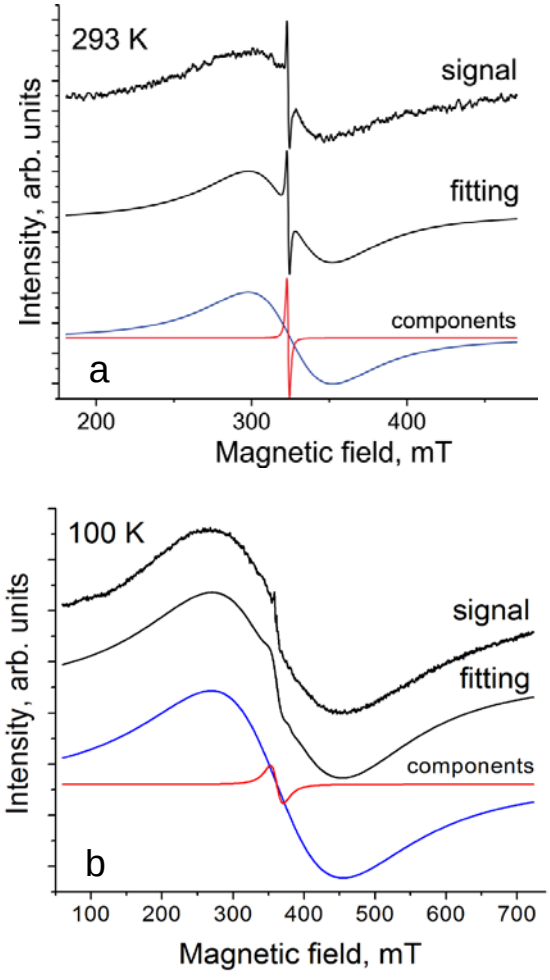

Fig. 5. EPR signal of polycrystalline **1** at 295 K (a) and **2** at 100 K (b). Fitting of the signal by two Lorentzian lines is shown below by red and blue curves.

and the parameters of the signal at 4.2 K are g = 2.0188 and ΔH = 81.8 mT. On the background of the broad signal, a narrow component was also observed. It has g = 1.9974 and ΔH= 1.61 mT at 293 K (Fig. 5a). The g-factor and the linewidth of this component were nearly temperature independent down to 4.2 K. This component can be attributed to the reduced $Pc^{\bullet 3-}$ macrocycle according to the g-factor value and linewidth.[12, 19, 25, 26] However, integral intensity of this component is only 0.1% from that of the broad signal. That allows one to conclude that spin density is localized mainly on V^{II} in **1**. In spite of similar geometry of $[V^{II}(MeIm)_2(Pc^{2-})]$ units in **1** and **2,** they show different EPR signals. A very broad (ΔH = 141.8 mT) EPR signal in **2** with g =1.7359 and ΔH = 178.9 mT at 293 K can also be attributed to V^{II}. This signal shifts to higher g-factors and slightly narrows with the temperature decrease, and the parameters of the signal at 4.2 K are g = 1.8300 and ΔH = 161.0 mT (spectrum of **2** at 100 K is shown in Fig. 5b). A narrow component was also observed in **2** (Fig. 5b) and its integral intensity is even less than 0.1% from that of the broad signal.

Generally, EPR signals from Cr^{II} are not observed due to large linewidth.[27] However, in the case of **3**, we observed a broad intense EPR signal with g = 2.0534 and ΔH= 60.3 mT at

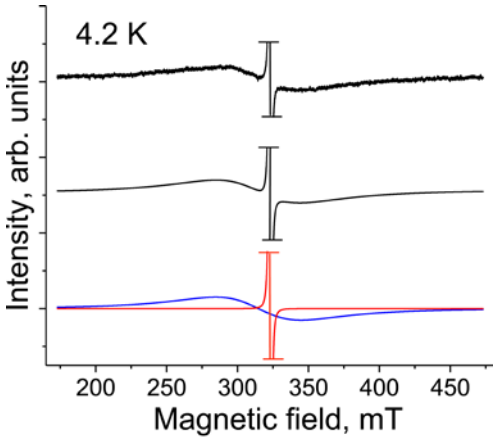

Fig. 6. EPR signal from polycrystalline **3** at 4.2 K.

4.2 K which can be attributed to Cr^{II} (Fig. 6). A narrow component was also observed in the spectrum of **3**. The values g = 2.0002 and ΔH = 0.88 mT at 4.2 K allow it to be attributed to $Pc^{\bullet 3-}$. Integral intensity of the narrow component is less

than 0.1% from that of the broad signal. Thus, EPR data show that spin density is localized on paramagnetic metal atoms and charge transfer from metal to the Pc macrocycle is nearly absent since the content of $Pc^{\bullet 3-}$ is less than 0.1% in **1**–**3**. Compound **4** with $[Fe^{II}(MeIm)_2(Pc^{2-})]$ is EPR silent most probably due to the formation of diamagnetic Fe^{II} (S = 0) and Pc^{2-} species. Previously it was shown that pyridine complex $[Fe^{II}(Py)_2(Pc^{2-})]$ also contains low spin Fe^{II} (S = 0).[14]

e. Theoretical analysis

To clarify electronic structures in $[V(MeIm)_2Pc]^0$ and $[Cr(MeIm)_2Pc]^0$, theoretical analyses were performed at the CAM-B3LYP/cc-pVTZ/cc-pVDZ level of theory, where partial geometry optimizations on the hydrogen atoms only were carried out from the X-ray structures of **1** and **3**, respectively. The total and relative energies, $\langle S^2 \rangle$ values, and charge and spin density in $[V(MeIm)_2Pc]^0$ and $[Cr(MeIm)_2Pc]^0$ are summarized in Tables S2 and S3. The ground states were the quartet and triplet states for $[V(MeIm)_2Pc]^0$ and $[Cr(MeIm)_2Pc]^0$, respectively, which is consistent with the observed magnetic moments. In both $[V(MeIm)_2Pc]^0$ and $[Cr(MeIm)_2Pc]^0$, the main spin densities stem from 3d orbitals of the central transition metals. However, the sign of spin density on Pc moiety was polar opposite between $[V(MeIm)_2Pc]^0$ and $[Cr(MeIm)_2Pc]^0$ (Fig. 7 and Table S3). The non-spin-projected and spin-projected diradical characters y_i and y_i^{SP} (i = 0 and 1) were estimated from the occupation numbers of paired natural orbitals, n(HO−i) and n(LU+i).[28]

$$y_i = n(\mathrm{LU}+i) = 2 - n(\mathrm{HO}-i) \quad (1)$$

$$y_i^{SP} = n^{SP}(\mathrm{LU}+i) = 2 - n^{SP}(\mathrm{HO}-i)$$
$$= [n(\mathrm{LU}+i)]^2/(1 + S_i^2) = 2 - [n(\mathrm{HO}-i)]^2/(1 + S_i^2) \quad (2)$$

$$S_i = [n(\mathrm{HO}-i) - n(\mathrm{LU}+i)]/2 \quad (3)$$

The diradical characters y_i and y_i^{SP} range from 0 (closed-shell) to 1 (pure diradical). The $y_0^{(SP)}$ and $y_1^{(SP)}$ values are indices of the diradical and tetraradical, respectively, e.g., $y_0^{(SP)} = y_1^{(SP)} = 0$ (closed-shell); $y_0^{(SP)} = 1$, $y_1^{(SP)} = 0$ (pure diradical); $y_0^{(SP)} = y_1^{(SP)} = 1$ (pure tetraradical). The values $y_0^{(SP)}$ and $y_1^{(SP)}$ in $[V(MeIm)_2Pc]^0$ were almost zero. The $y_1^{(SP)}$ in $[Cr(MeIm)_2Pc]^0$ is also almost zero but the value $y_0^{(SP)}$ of 0.285 shows that the diradicaloid character of $[Cr(MeIm)_2Pc]^0$ is induced and they are comparable to those in aromatic hydrocarbon heptacene. The diradicaloid character is related to negative spin density on the Pc moiety in $[Cr(MeIm)_2Pc]^0$ and the bonds alternation in the Pc macrocycle of **3**, as it is characteristic of $Pc^{\bullet 3-}$ (Table 1).

The energy diagrams for the frontier Kohn–Sham orbitals of the ^4A_g state in $[V(MeIm)_2Pc]^0$ and the ^3A_g state in $[Cr(MeIm)_2Pc]^0$ are shown in Figs. S7 and S8, respectively.

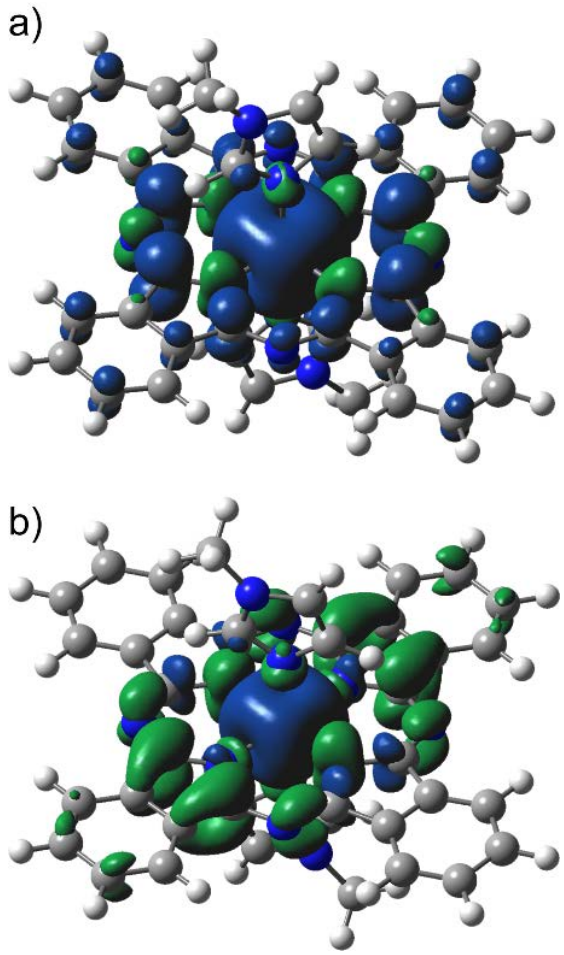

Fig. 7. The isosurface plots for spin density distribution. (a) The ^4A_g state in $[V(MeIm)_2Pc]^0$ and (b) the ^3A_g state in $[Cr(MeIm)_2Pc]^0$, where the isosurface value is 0.0016 electron/au^3. The isosurfaces in blue and green denote positive and negative spin density, respectively.

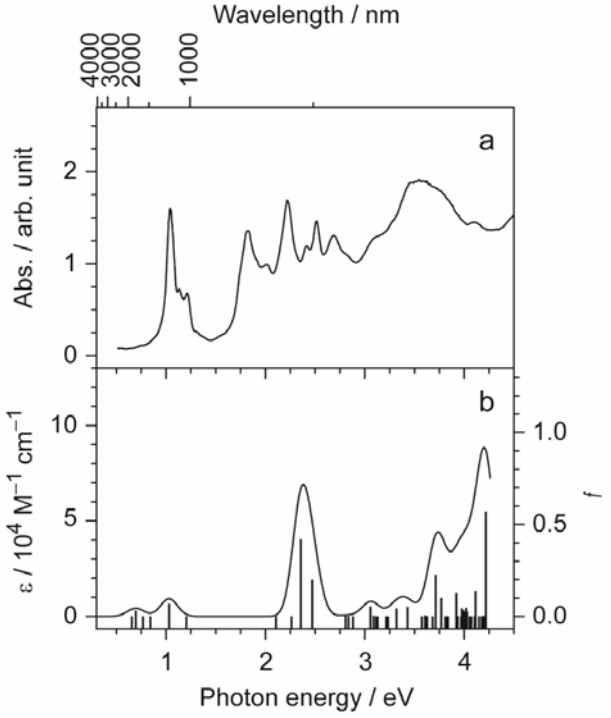

Fig. 8. (a) Observed UV-vis-NIR spectrum of $[V(MeIm)_2Pc]\cdot 2C_6H_4Cl_2$ (**2**) in KBr. (b) Calculated spectrum of the ^4A_g state in $[V(MeIm)_2Pc]^0$ at the CAM-B3LYP/cc-pVTZ/cc-pVDZ level of theory.

Based on the time-dependent density functional theory (TD-DFT) at the same level of theory, the calculated excitation energies, oscillator strengths, $\langle S^2 \rangle$ values, and assignments on the low-lying excited states of $[V(MeIm)_2Pc]^0$ and $[Cr(MeIm)_2Pc]^0$ are summarized in Tables S5 and S6. The observed and calculated UV-vis-NIR spectra are compared in Figs. 8 and 9.

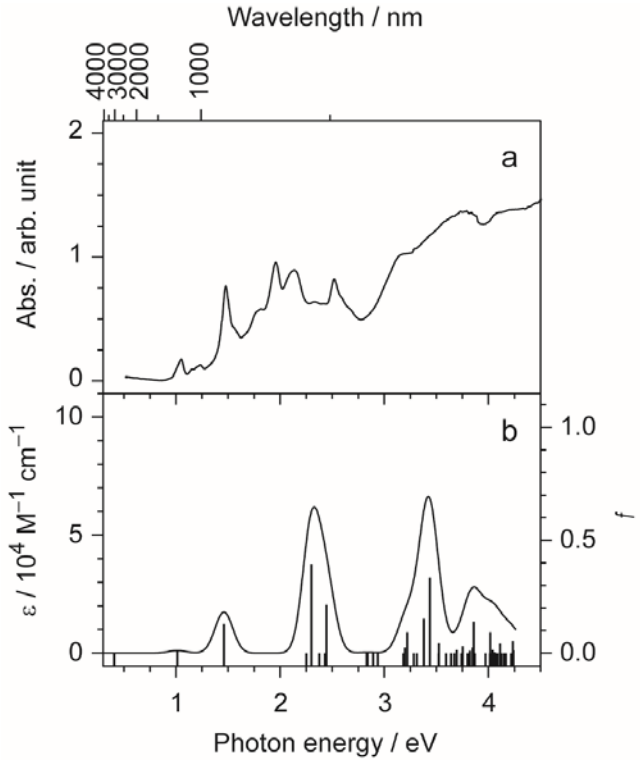

Fig. 9. (a) Observed UV-vis-NIR spectrum of $[Cr(MeIm)_2Pc]\cdot 2C_6H_4Cl_2$ (**3**) in KBr. (b) Calculated spectrum of the ^3A_g state in $[Cr(MeIm)_2Pc]^0$ at the CAM-B3LYP/cc-pVTZ/cc-pVDZ level of theory.

Comparing the observed UV-vis-NIR spectrum with the calculated one in $[V(MeIm)_2Pc]^0$, the present TD-DFT calculation predicted six excited states in the range from 0.655 eV to 1.204 eV, and the lowest energy band at 1.04 eV (1187 nm) can be assigned as the the *β*-HO → *β*-LU and/or *β*-HO → *β*-(LU+1) excitations based on the oscillator strengths, which correspond to the second and fifth excited states, respectively (Table S5). On the other hand, the calculated spectral feature in $[Cr(MeIm)_2Pc]^0$ was significantly different from that in $[V(MeIm)_2Pc]^0$ (Table S6). The first excited state is the *β*-HO → *β*-LU excitation of low intensity at very low energy of 0.407 eV. The second excited state is the *α*-HO ⟶ *α*-(LU+1)/LU and *β*-(HO-1) ⟶ *β*-LU excitations at 1.012 eV, and the third excited state is the *α*-HO ⟶ *α*-LU/(LU+1) excitations at 1.460 eV, the characters of which orbital involved are similar to the second and fifth excited states in $[V(MeIm)_2Pc]^0$. As for the *β*-HO → *β*-LU excitation in $[Cr(MeIm)_2Pc]^0$, both orbitals concerned and the excitation energy are not essentially the same as those in $[V(MeIm)_2Pc]^0$, which would be related to the bond alternation and the diradicaloid character of the Pc moiety in $[Cr(MeIm)_2Pc]^0$. Comparing the observed and calculated spectra, the bands at 1.05 eV (1178 nm) and 1.48 eV (841 nm) can be assigned as the *α*-HO ⟶ *α*-(LU+1)/LU and *β*-(HO-1) ⟶ *β*-LU and the *α*-HO ⟶ *α*-LU/(LU+1) excitations, which correspond to the second and the third excited states, respectively (Table S6).

Open-shell singlet diradicaloid state when frontier orbitals are distributed in different space of the molecule produces unpaired spin density is a very interesting phenomenon. Such molecules generally have small HOMO–LUMO energy gap, can show relatively high conductivity of semiconducting type and in some cases manifest temperature induced EPR signals.[29,30] Such states manifest π-extended aromatic hydrocarbon molecules (polyacenes, biphenalenes, anthenes, and zenthrenes),[29] *o*- and *p*-quinodimethanes[30]. Due to the ability to populate closely lying excited triplet state in these molecules they are promising compounds to develop pure organic magnetic systems.[31] However, among macroheterocycles which also have large π-electron system, open shell singlet diradicaloid is very rare. It was shown that some nickel(II) and copper(II) corroles have diradical character.[17] Synthesis and anomalous properties of the oxidized doubly linked corrole dimer and its zinc(II) complex which exhibit singlet diradical character were reported.[18] Our work shows that in some cases the Pc macrocycles can manifest the sign of diradicaloid providing unusual optical properties of metal phthalocyanines.

EXPERIMENTAL

Materials

N-methylimidazole (MeIm, Aldrich, 98%), and $[V^{IV}OPc]^0$ (Acros, 85%), $[Sn^{IV}Cl_2Pc]^0$ (TCI reagents), $Fe^{II}Pc$ (Aldrich, >90%), $In^{III}ClPc$ (Aldrich, 95%) were used as received. Chromium(III) chloride phthalocyanine was obtained from $Cr^{III}Cl_3\cdot 3THF$ and *o*-dicyanobenzene and purified as described in Ref. 32 for preparation of $Ti^{IV}Cl_2Pc$. Chromium(II) chloride (99.99%) and samarium(II) iodide (99.9%) were purchased from Aldrich. Sodium fluorenone ketyl was obtained according to Ref. 33. Solvents were purified under argon atmosphere and degassed. *o*-Dichlorobenzene ($C_6H_4Cl_2$) was distilled over CaH_2 under reduced pressure and *n*-hexane was distilled over Na/benzophenone. All manipulations for the syntheses of **1**–**4** were carried out in an MBraun 150B-G glove box with controlled argon atmosphere and the content of H_2O and O_2 less than 1 ppm. The solvents and crystals were stored in the glove box. Polycrystalline samples of **1**–**4** were placed in 2 mm quartz tubes in anaerobic conditions for EPR and SQUID measurements and sealed under 10^{-5} torr pressure. KBr pellets for IR and UV-visible-NIR measurements of **1**–**4** were prepared in the glove box.

General

UV-visible-NIR spectra were measured in KBr pellets on a UV-visible-NIR spectra were measured in KBr pellets on a Perkin Elmer Lambda 1050 spectrometer in the 250–2500 nm range. FT-IR spectra were obtained in KBr pellets with a Perkin-Elmer Spectrum 400 spectrometer (400-7800 cm^{-1}). EPR spectra were recorded for polycrystalline samples of **1**–**4** with a JEOL

JES-TE 200 X-band ESR spectrometer equipped with a JEOL ES-CT470 cryostat working between room and liquid helium temperatures. A Quantum Design MPMS-XL SQUID magnetometer was used to measure static magnetic susceptibility of **1**–**3** at 100 mT magnetic field in cooling and heating conditions in the 300 − 1.9 K range. A sample holder contribution and core temperature independent diamagnetic susceptibility (χ_d) were subtracted from the experimental values. The χ_d values were estimated by the extrapolation of the data in the high-temperature range by fitting the data with the expression: $\chi_M = C/(T - \Theta) + \chi_d$, where C is Curie constant and Θ is Weiss temperature. Effective magnetic moment (μ_{eff}) was calculated with the following formula: $\mu_{eff} = (8 \cdot \chi_M \cdot T)^{1/2}$.

Synthesis

Crystals of **1**–**4** were obtained by diffusion technique. A reaction mixture was filtered into a 1.8-cm-diameter, 50 mL glass tube with a ground glass plug, and then 30 mL of *n*-hexane was layered over the solution. Slow mixing of the solutions resulted in precipitation of crystals over 1 month. The solvent was then decanted from the crystals, and they were washed with *n*-hexane. The compositions of the obtained salts were determined from X-ray diffraction analysis on a single crystal. Several crystals from one synthesis were found to consist of a single crystalline phase. Due to air sensitivity of **1** and **2**, elemental analysis could not be used to confirm the composition because the salts reacted with oxygen in the air before the quantitative oxidation procedure could be performed.

$[V^{II}(MeIm)_2(Pc^{2-})]^0 \cdot MeIm$ (**1**) was obtained by the reduction of vanadyl(IV) phthalocyanine ($V^{IV}OPc$, 24.4 mg, 0.042 mmol) by 2.3 equivalents of sodium fluorenone ketyl (20 mg, 0.098 mmol) in the presence of two equivalents of samarium(II) iodide (34 mg, 0.084 mmol) in 16 ml of $C_6H_4Cl_2$ with an addition of 0.2 ml of *N*-methylimidazole upon stirring the solution at 80°C. First, the solution turned deep blue, and violet-brown solution was obtained in two hours, which was cooled down to room temperature and filtered into the tube for diffusion. Crystals of **1** were obtained as metallic black blocks of large size in 62% yield (the size of crystals up to 1×1×1 mm^3). We also found that reduction of $V^{IV}OPc$ in the presence of *N*-methylimidazole can be carried out by two equivalents of $Sm^{II}I_2$ only. However, in this case reduction is realized at an essentially lower rate (totally 24 hours are needed to dissolve $V^{IV}OPc$ and form brown violet solution).

$[V^{II}(MeIm)_2(Pc^{2-})]^0 \cdot 2C_6H_4Cl_2$ (**2**) was obtained by the reduction of vanadyl(IV) phthalocyanine ($V^{IV}OPc$, 24.4 mg, 0.042 mmol) by 2.3 equivalents of sodium fluorenone ketyl (20 mg, 0.098 mmol) and an excess of chromium(II) chloride (20 mg, 0.105 mmol) in 16 ml of $C_6H_4Cl_2$ with an addition of 0.2 ml of *N*-methylimidazole during 8 hours at 80°C. First, the solution turned deep blue but after four hours violet-brown solution was obtained, which was cooled down to room temperature and filtered into the tube for diffusion. Crystals of **2** were obtained as black blocks in 51 % yield. The same reaction is realized at essentially lower rate even without sodium fluorenone ketyl when only $Cr^{II}Cl_2$ is used as reductant. In this case the reaction is accomplished in 24 hours.

After filtration of brown violet solution of $[V^{II}(MeIm)_2(Pc^{2-})]^0$ in *o*-dichlorobenzene we tried to reduce this compound by excess of sodium fluorenone ketyl in the presence of one equivalent of cryptand[2.2.2]. The reaction was accompanied by immediate color change from brown-violet to deep blue indicating the restoration of oxygen ligand. Indeed, the crystals of known salt were isolated from this solution which have the unit cell parameters found previously for the $[cryptand[2.2.2](Na^+)][V^{IV}O(Pc^{\bullet 3-})]^{\bullet -} \cdot C_6H_4Cl_2$ [19] salt.

$[Cr^{II}(MeIm)_2(Pc^{2-})]^0 \cdot 2C_6H_4Cl_2$ (**3**) was obtained by the reduction of chromium(III) chloride phthalocyanine ($Cr^{III}ClPc$, 25 mg, 0.042 mmol) by an excess of chromium(II) chloride (16 mg, 0.084 mmol) in 16 ml of $C_6H_4Cl_2$ with an addition of 0.2 ml of *N*-methylimidazole during two days at 80°C. The reaction yielded green-blue solution which was cooled down to room temperature and then filtered into the tube for diffusion. Crystals of **3** were obtained as metallic black rhombs in 43 % yield. Composition of the crystals was confirmed by elemental analysis: Anal. Calcd for $C_{52}H_{36}Cl_4CrN_{12}$, M_r = 1022.73: C 61.01, H 3.52, N 16.42; Cl 13.88; Found: C 60.84, H 3.44, N 16.21, Cl 13.24. Similar crystals can be obtained at the reduction of $Sn^{IV}Cl_2Pc$ or $In^{III}ClPc$ by chromium(II) chloride in the presence of *N*-methylimidazole. These crystals have unit cell parameters and geometry of the components as well as IR and UV-visible-NIR spectra similar to that of **3**. These data show that chromium easily substitutes $Sn^{IV}Cl_2$ and $In^{III}Cl$ forming the crystals of $[Cr^{II}(MeIm)_2(Pc^{2-})] \cdot 2C_6H_4Cl_2$ (**3**).

Good quality single crystals of $[Fe^{II}(MeIm)_2(Pc^{2-})]^0 \cdot 2C_6H_4Cl_2$ (**4**) were obtained at the dissolution of iron(II) phthalocyanine ($Fe^{II}Pc$, 24 mg, 0.042 mmol) in 16 ml of $C_6H_4Cl_2$ with an addition of 0.2 ml of *N*-methylimidazole during one day at 80°C. The reaction yielded green solution which was cooled down to room temperature and filtered into the tube for diffusion. Crystals of **4** were obtained as metallic black blocks of large size (up to 1×1×0.5 mm^3) in 74 % yield. Composition of the crystals was confirmed by elemental analysis: Anal. Calcd for $C_{52}H_{36}Cl_4FeN_{12}$, M_r = 1026.58: C 60.84, H 3.51, N 16.37; Cl 13.83; Found: C 61.46, H 3.42, N 16.08, Cl 13.16.

X-ray crystal structure determination

Crystal data of **1** at 150(2) K: $C_{44}H_{34}N_{14}V$, M_r = 809.79 g mol^{-1}, black block, monoclinic, $P\ 2_1/c$, a = 19.1243(6), b = 11.2003(2), c = 18.9602(5) Å, β = 109.715(3)°, V = 3823.17(19) Å^3, Z = 4, d_{calc} = 1.407 g·cm^{-3}, μ = 0.314 mm^{-1}, $F(000)$ = 1676, $2\theta_{max}$ = 59.090°, reflections measured 45443, unique reflections 9733, reflections with $I > 2\sigma(I)$ = 6895, parameters refined 558, restraints 13, R_1 = 0.0457, wR_2 = 0.1087, G.O.F. = 1.017, CCDC 1821123.

Crystal data of **2** at 130(2) K: $C_{52}H_{36}Cl_4N_{12}V$, M_r = 1021.67 g mol^{-1}, black block, monoclinic, $P\ 2_1/c$, a = 13.7115(2), b = 17.6061(2), c = 9.56080(10) Å, β = 100.5380(10)°, V = 2269.11(5) Å^3, Z = 2, d_{calc} = 1.495 g·cm^{-3}, μ = 0.509 mm^{-1}, $F(000)$ = 1046, $2\theta_{max}$ = 66.038°, reflections measured 34580, unique reflections 7927, reflections with $I > 2\sigma(I)$ = 6844, parameters refined 313, restraints 0, R_1 = 0.0336, wR_2 = 0.0900, G.O.F. = 1.044, CCDC 1821124.

Crystal data of **3** at 150(2) K: $C_{52}H_{36}Cl_4CrN_{12}$, M_r = 1022.73 g mol^{-1}, black rhombohedral plate, monoclinic, $C\ 2/c$, a =

24.7918(9), *b* = 10.5704(3), *c* = 18.1334(7) Å, β = 108.240(4)°, *V* = 4513.3(3) Å^3, *Z* = 4, d_{calc} = 1.505 g·cm^{-3}, μ = 0.545 mm^{-1}, *F*(000) = 2095, $2\theta_{max}$ = 58.986°, reflections measured 12816, unique reflections 5301, reflections with $I > 2\sigma(I)$ = 4185, parameters refined 339, restraints 18, R_1 = 0.0428, wR_2 = 0.1162, G.O.F. = 1.065, CCDC 1821125.

Crystal data of **4** at 150(2) K: $C_{52}H_{36}Cl_4FeN_{12}$, M_r = 1026.58 g mol^{-1}, black block, monoclinic, *C* 2/c, *a* = 24.6494(13), *b* = 10.6126(4), *c* = 18.1082(8) Å, β = 108.584(5)°, *V* = 4490.0(4) Å^3, *Z* = 4, d_{calc} = 1.519 g·cm^{-3}, μ = 0.629 mm^{-1}, *F*(000) = 2104, $2\theta_{max}$ = 56.372°, reflections measured 18896, unique reflections 4804, reflections with $I > 2\sigma(I)$ = 4257, parameters refined 364, restraints 31, R_1 = 0.0548, wR_2 = 0.1681, G.O.F. = 1.065, CCDC 1821126.

The data for **1**–**4** were collected on an Oxford diffraction "Gemini-R" CCD diffractometer with graphite monochromated MoKα radiation using an Oxford Instrument Cryojet system. Raw data reduction to F^2 was carried out using CrysAlisPro, Oxford Diffraction Ltd.[34] The structures were solved by direct method and refined by the full-matrix least-squares method against F^2 using SHELX 2014/7 and 2016/6[35] and Olex2[36]. Non-hydrogen atoms were refined in the anisotropic approximation. Positions of hydrogen atoms were calculated geometrically. Crystal structure of **1** contains two halves of independent [V^{II}(MeIm)$_2$(Pc^{2-})] units and one independent non-coordinated MeIm molecule. This molecule is disordered between two orientations with the 0.842(14)/0.158(14) occupancies. Crystal structure of **2** contains half of independent [V^{II}(MeIm)$_2$(Pc^{2-})] and one independent ordered solvent $C_6H_4Cl_2$ molecule. Methyl group of coordinated MeIm is statistically rotationally disordered between two orientations in **2**. Crystal structure of **3** contains solvent $C_6H_4Cl_2$ molecules disordered between two orientations with the 0.9521(12)/0.0479(12) occupancies. The MeIm ligand coordinated to the iron(II) atoms has two positions in the crystal structure of **4** related by the rotation of the molecule by ~180° about the coordinated N-Fe bond with the 0.905(8)/0.095(8) occupancies. The $C_6H_4Cl_2$ molecule is also disordered in **4** with the 0.8966(18)/0.1034(18) occupancies.

Theoretical calculations

DFT and TD-DFT calculations based on the CAM-B3LYP functional[37] were performed using the cc-pVDZ (C, H, and N)[38] and cc-pVTZ (V and Cr)[39] basis sets. Partial geometry optimizations on the coordinates of hydrogen atoms in C_i-symmetric [V(MeIm)$_2$Pc]^0 and [Cr(MeIm)$_2$Pc]^0 were performed based on the X-ray structures, in which "Opt = Tight" was specified. In the present calculations, "Int =SuperFineGrid" was specified, and stabilities of the wave functions were confirmed by specifying the "Stable = Opt" keyword. Fifty excited states were calculated in the TD-DFT calculation. The subsequent natural bond orbital (NBO) analysis was performed using the NBO program.[40] The computations were performed with the Gaussian 09 program package.[41]

Conclusions

The series of the MeIm solvates of vanadium(II), chromium(II) and iron(II) phthalocyanines [M^{II}(MeIm)$_2$(Pc^{2-})]^0·Solvent (**1**–**4**) were obtained allowing their structures, optical and magnetic properties to be studied. These phthalocyanines were obtained by the reduction of oxo- and halide metal(IV) or metal(III) phthalocyanines in the presence of MeIm by Cr^{II}Cl$_2$ and Sm^{II}I$_2$ together with or without sodium fluorenone ketyl as a reductant. The MeIm ligands coordinated to metal atoms from both sides of the macrocycle providing the formation of metals in the distorted octahedral environment. The shortest M–N(MeIm) and M–N(Pc) bonds formed with Fe^{II}Pc are elongated for Cr^{II}Pc and the longest bonds are observed for V^{II}Pc. It is shown that metal atoms preserve +2 oxidation state and the Pc macrocycles have –2 charge. No effective charge transfer from metal to the Pc macrocycle is proved by the weak signals from Pc$^{\bullet 3-}$ observed in the spectra of the complexes. Upon the coordination of strong ligands, metals lower spin multiplicity as observed for Cr^{II}Pc and Fe^{II}Pc. However, vanadium(II) preserves high *S* = 3/2 spin state in the [M^{II}(MeIm)$_2$(Pc^{2-})]^0 units. In spite of the absence of Pc$^{\bullet 3-}$ in **1**–**3**, they show strong absorption in the NIR range that is explained by unusually small HOMO–LUMO gaps for V^{II}Pc and Cr^{II}Pc in the MeIm solvates. Moreover, V^{II}Pc and Cr^{II}Pc manifest multiple bands in visible range. DFT calculations demonstrate essential diradicaloid character for the Pc macrocycle in [Cr^{II}(MeIm)$_2$(Pc^{2-})]^0 comparable to that of π-extended aromatic hydrocarbon heptacene which also shows diradicaloid character. Thus, like corroles the Pc macrocycles can manifest diradicaloid character providing promising optical and magnetic properties.

Aknowledgements

The work was supported by Russian Science Foundation (project № 17-13-01215), by a Grant-in-Aid for Scientific Research on Innovative Areas "π-System Figuration: Control of Electron and Structural Dynamism for Innovative Functions" from Japan Society for the Promotion of Science (JSPS) JP17H05153, by JSPS KAKENHI Grant Number JP26288035 and JST (ACCEL) 27 (100150500010). Theoretical calculations were performed at the Super Computer System, Institute for Chemical Research, Kyoto University, and the Research Center for Computational Science, Okazaki, Japan.

References

1 C. G. Claessens, W. J. Blau, M. Cook, M. Hanack, R. J. M. Nolte, T. Torres and D. Wöhrle, *Monat. Chem.* 2001, **132**, 3.
2 D. Wöhrle, G. Schnurpfeil, S. G.; Makarov, A. Kazarin and O.N. Suvorova, *Macroheterocycles*, 2012, **5**, 191.
3 J. L. Petersen, C. S. Schramm, D. R. Stojakovic, B. M. Hoffman and T. J. Marks, *J. Am. Chem. Soc*., 1977, **99,** 286.
4 H. Hasegawa, T. Naito, T. Inabe, T. Akutagawa and T. Nakamura, *J. Mater. Chem*., 1998, **8**, 1567.
5. T. Inabe and H. Tajima, *Chem. Rev*., 2004, **104**, 5503.
6 J. S. Miller, C. Vazquez, J. C. Calabrese, M. L. McLean and A. Epstein, J. *Adv. Mater.,* 1994, **6**, 217.
7 D. V. Konarev, L. V. Zorina, S. S. Khasanov, E. U. Hakimova and R. N.

Lyubovskaya, *New J. Chem*., 2012, **36**, 48.
8 J. A. Cissell, T. P. Vaid and A. L. Rheingold, *Inorg. Chem.,* 2006, **45,** 2367.
9 D. V. Konarev, A. V. Kuzmin, S. S. Khasanov, A. Otsuka, H. Yamochi, G. Saito and R. N. Lyubovskaya, *Eur. J. Inorg. Chem.* 2016, 4099.
10 J. A. Cissell, T. P. Vaid, A. G. DiPasquale and A. L. Rheingold, *Inorg. Chem.,* 2007, **46**, 7713.
11 W. Zhou, R. H. Platel, T. T. Tasso, T. Furuyama, N. Kobayashi and D. B. Leznoff, *Dalton Trans.,* 2015, **44***,* 13955.
12 D. V. Konarev, A. V. Kuzmin, S. S. Khasanov, M. Ishikawa, A. Otsuka, H. Yamochi, G. Saito and R. N. Lyubovskaya, *Dalton Trans*., 2016, **45**, 10780.
13 J. Janczak, R. Kubiak, M. Śledź, H. Borrmann, Y. Grin, *Polyhedron,* 2003, **22**, 2689.
14 J. Janczak and R. Kubiak, *Inorg. Chim. Acta***,** 2003, **342,** 64–76.
15 A.B.P. Lever, *J. Chem. Soc. (London),* 1965, 1821.
16 W. Zhou, J. R. Thompson, C. C. Leznoff and D. B. Lez, *Chem. Eur. J.,* 2017, **23**, 2323.
17 (a) S. Will, J. Lex, E. Vogel, H. Schmickler, J. P. Gisselbrecht, C. Haubtmann, M. Bernard and M. Gross, *Angew. Chem., Int. Ed. Engl.,* 1997, **36**, 357; (b) F. Jérôme, J.-M. Barbe, C. P. Gros, R.; Guilard, J. Fisher and R.Weiss, *New J. Chem.,* 2001, **25**, 93.
18 S. Hiroto, K. Furukawa, H. Shinokubo and A. Osuka, *J. Am. Chem. Soc*., 2006, **128**, 12380.
19 D. V. Konarev, M. A. Faraonov, A. V. Kuzmin, S. S. Khasanov, Y. Nakano, M. S. Batov, S. I. Norko, A. Otsuka, H. Yamochi, G. Saito and R. N. Lyubovskaya, *New J. Chem.,* 2017, **41**, 6866.
20. M. Szostak, M. Spain and D.J. Procter, *J. Org. Chem.* 2014, **79**, 2522.
21 (a) E. W. Y. Wong, C. J. Walsby, T. Storr and D. B. Leznoff, *Inorg. Chem.*, 2010, **49**, 3343; (b) D.V. Konarev, A.V. Kuzmin, S.S. Khasanov, M. S. Batov, A. Otsuka, H. Yamochi, H. Kitagawa and R. N. Lyubovskaya, *CrystEngComm*., 2018, **20**, 385.
22 A. J. Ramadan, L. A. Rochford, D. S. Keeble, P. Sullivan, M. P. Ryan, T. S. Jones and S. Heutz, *J. Mater. Chem. C*, 2015, **3**, 461.
23 D. V. Konarev, A. V. Kuzmin, S. V. Simonov, S. S. Khasanov and R. N. Lyubovskaya, *J. Porph. Phth*., 2014, **18**, 87.
24 (a) B. N. Figgis and R. S. Nyholm, *J. Chem. Soc.*,1959, 338; (b) B. W. Dale, R. J. P. Williams and T. L. Throp, *J. Chem. Phys*. 1965, **49**, 3441.
25 D. V. Konarev, A. V. Kuzmin, M. A. Faraonov, M. Ishikawa, Y. Nakano, S. S. Khasanov, A. Otsuka, H. Yamochi, G. Saito and R. N. Lyubovskaya, *Chem. Eur. J.,* 2015, **21**, 1014.
26 (a) D. V. Konarev, L. V. Zorina, S. S. Khasanov, A. L. Litvinov, A. Otsuka, H. Yamochi, G. Saito and R. N. Lyubovskaya, *Dalton Trans.,* 2013, **42**, 6810; (b) D. V. Konarev, S. S. Khasanov, M. Ishikawa, A. Otsuka, H. Yamochi, G. Saito and R. N. Lyubovskaya, *Dalton Trans.,* 2017, 46, 3492.
27 A. Pénicaud, J. Hsu, C. A. Reed, A. Koch, K. C. Khemani, P. -M. Allemand and F. Wudl. *J. Am. Chem. Soc.,* 1991, **113**, 6698.
28 a) M. Nakano, H. Fukui, T. Minami, K. Yoneda, Y. Shigeta, R. Kishi, B. Champagne, E. Botek, T. Kubo, K. Ohta and K. Kamada, *Theor. Chem. Acc.,* 2011, **130**, 711; b) M. Nakano, T. Minami, H. Fukui, K. Yoneda, Y. Shigeta, R. Kishi, B. Champagne and E. Botek, *Chem. Phys. Lett.,* 2010, **501**, 140; c) K. Yoneda, M. Nakano, Y. Inoue, T. Inui, K. Fukuda, Y. Shigeta, T. Kubo and B. Champagne, *J. Phys. Chem. C* 2012, **116**, 17787.
29 (a) M. Bendikov, H. M. Duong, K. Starkey, K. N. Houk, E. A. Carter, F. Wudl, *J. Am. Chem. Soc*., 2004, **126**, 7416; (b) A. Shimizu, T. Kubo, M. Uruichi, K. Yakushi, M. Nakano, D. Shiomi, K. Sato, T. Takui, Y. Hirao, K. Matsumoto, H. Kurata, Y. Morita and K. Nakasuji, *J. Am. Chem. Soc*., 2010, **132**, 14421.
30 L. K. Montgomery, J. C. Huffman, E. A. Jurczak and M. P. Grendze, *J. Am. Chem. Soc.,* 1986, **108**, 6004, and references cited therein.
31. Y. Zheng, M. Miao, G. Dantelle, N. D. Eisenmenger, G. Wu, I. Yavuz, M. Chabinyc, L. K. N. Houk and F. Wudl, *Adv. Mater.,* 2015, **27**, 1718.
32 L. A. Tomachynsk, V. Ya. Chernii and S. V. Volkov, *Russ. J. Inorg. Chem.,* 2002, **47**, 208.
33 D. V. Konarev, S. S. Khasanov, E. I. Yudanova and R. N. Lyubovskaya, *Eur. J. Inorg. Chem.,* 2011, 816.
34 Bruker AXS Inc., Madison, Wisconsin, USA.
35 G. M. Sheldrick, *Acta Crystallogr., Sect. A: Fundam. Crystallogr.,* 2008, **64**, 112.
36 O. V. Dolomanov, L. J. Bourhis, R. J. Gildea, J. A. K. Howard and H. Puschmann, *J. Appl. Cryst.,* 2009, **42**, 339.
37 T. Yanai, D. Tew and N. Handy, *Chem. Phys. Lett.,* 2004, **393**, 51.
38 T. H. Dunning, Jr. *J. Chem. Phys.,* 1989, **90**, 1007.
39 N. B. Balabanov and K. A. Peterson, *J. Chem. Phys.,* 2005, **123**, 064107.
40 NBO, Version 3.1, E. D. Glendening, A. E. Reed, J. E. Carpenter and F. Weinhold.
41 Gaussian 09, Revision E.01, M. J. Frisch, G. W. Trucks, H. B. Schlegel, G. E. Scuseria, M. A. Robb, J. R. Cheeseman, G. Scalmani, V. Barone, B. Mennucci, G. A. Petersson, H. Nakatsuji, M. Caricato, X. Li, H. P. Hratchian, A. F. Izmaylov, J. Bloino, G. Zheng, J. L. Sonnenberg, M. Hada, M. Ehara, K. Toyota, R. Fukuda, J. Hasegawa, M. Ishida, T. Nakajima, Y. Honda, O. Kitao, H. Nakai, T. Vreven, J. A. Montgomery, Jr., J. E. Peralta, F. Ogliaro, M. Bearpark, J. J. Heyd, E. Brothers, K. N. Kudin, V. N. Staroverov, T. Keith, R. Kobayashi, J. Normand, K. Raghavachari, A. Rendell, J. C. Burant, S. S. Iyengar, J. Tomasi, M. Cossi, N. Rega, J. M. Millam, M. Klene, J. E. Knox, J. B. Cross, V. Bakken, C. Adamo, J. Jaramillo, R. Gomperts, R. E. Stratmann, O. Yazyev, A. J. Austin, R. Cammi, C. Pomelli, J. W. Ochterski, R. L. Martin, K. Morokuma, V. G. Zakrzewski, G. A. Voth, P. Salvador, J. J. Dannenberg, S. Dapprich, A. D. Daniels, O. Farkas, J. B. Foresman, J. V. Ortiz, J. Cioslowski and D. J. Fox, Gaussian, Inc., Wallingford CT, 2013.

Graphic for TOC.

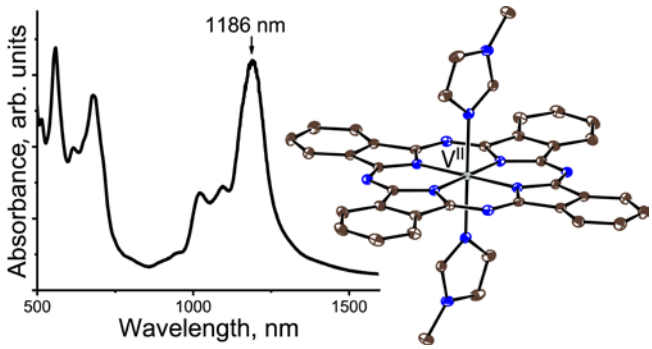

SYNOPSIS :

Crystal structures, optical and magnetic properties of *N*-methylimidazole (MeIm) solvates of vanadium(II), chromium(II) and iron(II) phthalocyanines: $[M^{II}(MeIm)_2(Pc^{2-})]^0$·Solvent (**1**–**4**) have been studied. Optical spectra of **1**–**3** ($V^{II}Pc$, $Cr^{II}Pc$) show absorption bands in the NIR range due to a small HOMO−LUMO gap in these phthalocyanines. The diradicaloid character of the Pc macrocycle is also shown in $[Cr^{II}(MeIm)_2(Pc^{2-})]^0$.

Supporting information.

Table S1. IR spectra of the compounds **1**–**4**.

Components	MeIm	$C_6H_4Cl_2$	$[V^{II}(MeIm)_2(Pc^{2-})]\cdot MeIm$ (**1**)	$[V^{II}(MeIm)_2(Pc^{2-})]\cdot 2C_6H_4Cl_2$ (**2**)	$[Cr^{II}(MeIm)_2(Pc^{2-})]\cdot 2C_6H_4Cl_2$ (**3**)	$[Fe^{II}(MeIm)_2(Pc^{2-})]\cdot 2C_6H_4Cl_2$ (**4**)
$M^{II}Pc$			441w	441w	439w	-
			505w	506w	507w	519w
			570w	570w	568w	570w
			728s	727s	725s	734s
			751s*	751s*	752s*	754s*
			-	-	761m	-
			772w	770w	776w	780w
			799w	800w	801w	-
			946w	946w	952w	947w
			1003w	1007w	1000w	1004w
			1057m	1057m	1076m*	1070m*
			1090s	1090s	1091m	1096s
			-	1100s	-	-
			1114s*	1115s*	1117s*	1120s*
			1164m	1166m	1166m	1165s
			1322s	1322s	1322m	1327m
			1405w	1405w	-	-
			1466s	1465s	1463s	1464w
			1535w	1534w	1534w	1530w
			1572w	1572w	1565w	1596w
			3055w	3055w	3051w	3057w
MeIm	620m		615w	616w	616w	614w
	666w		660w	659w*	660w*	662w*
	741m		751s*	751s*	752s*	754s*
	820m		817w	817w	819w	-
	905m		897w	897w	900w	899w
	1026w		-	-	-	-
	1077m		-	-	1076m*	1070m*
	1109m		1114s*	1115s*	1117s*	1120s*
	1230s		1234w	1236w	1237m	1240w
	1285m		1285m	1287m	1288m	1286m
	1358w		-	-	-	-
	1420m		-	1418w	1417m	1421s
	-		-	1433w	1435m	-
	1518s		1516w	1514w	-	1509s
	2919w		2920w	2918w	2921w	2920w
	2954w		-	-	2976w	2957w
	3110w		3116w	3116w	3117w	3118w
$C_6H_4Cl_2$		658w		659w*	660w*	662w*
		743m		751s*	752s*	754s*
		1033w		1033w	1033w	1033w
		1455s		1456m	1456s	1456w

w – weak, m-middle, s – strong intensity.

* - the bands are coincided.

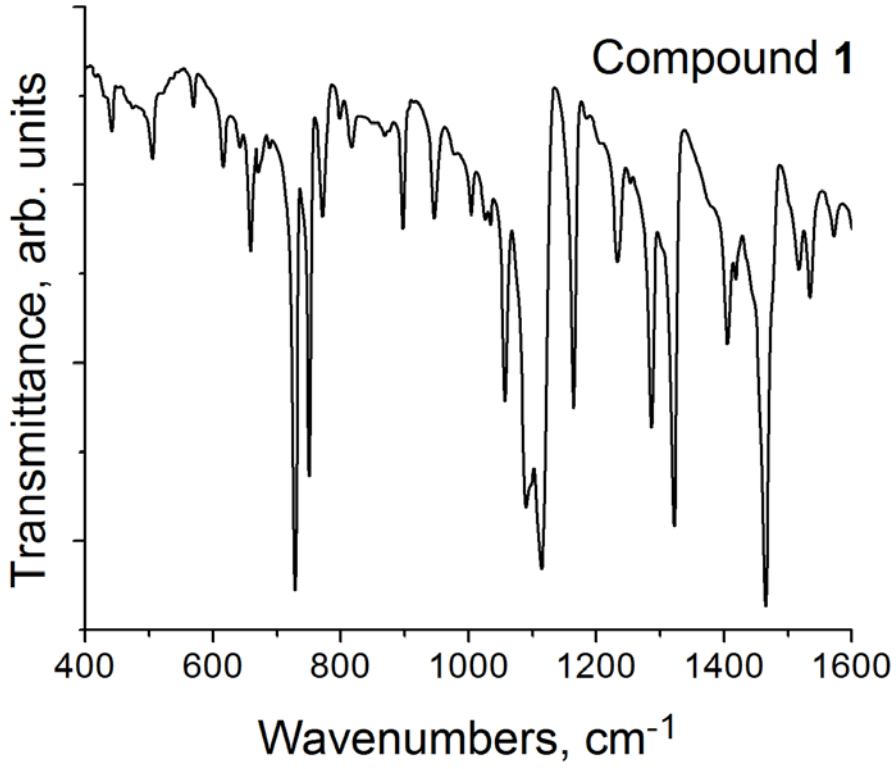

Fig. S1. IR spectrum of compound $[V^{II}(MeIm)_2(Pc^{2-})]\cdot MeIm$ (**1**) in KBr pellets. KBr pellet for **1** is prepared in anaerobic conditions.

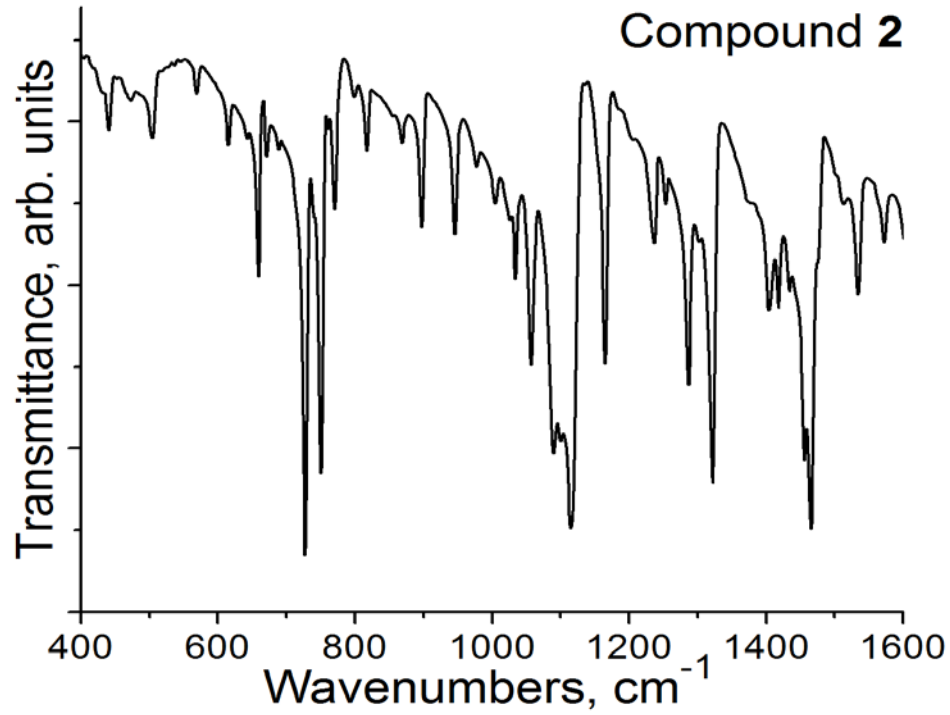

Fig. S2. IR spectrum of compound $[V^{II}(MeIm)_2(Pc^{2-})]\cdot 2C_6H_4Cl_2$ (**2**) in KBr pellets. KBr pellet for **2** was prepared in anaerobic conditions.

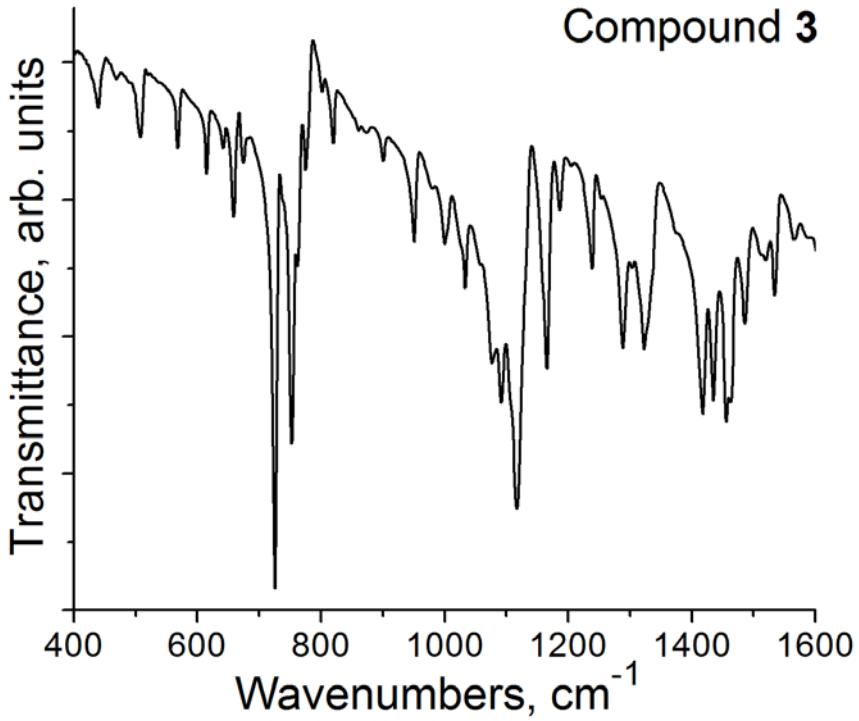

Fig. S3. IR spectrum of compound $[Cr^{II}(MeIm)_2(Pc^{2-})]\cdot 2C_6H_4Cl_2$ (**3**) in KBr pellets. KBr pellet for **3** was prepared in anaerobic conditions.

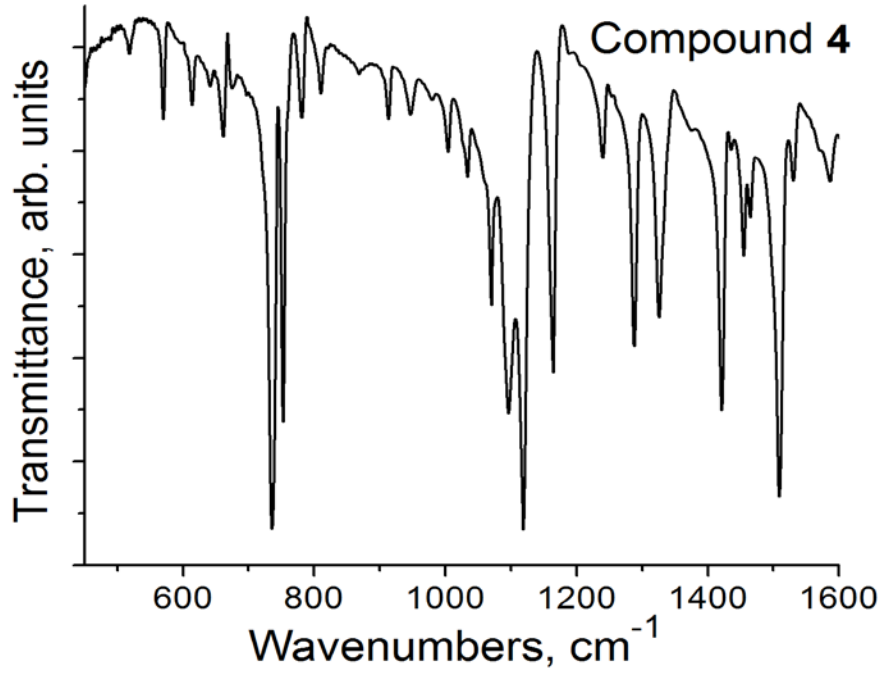

Fig. S4. IR spectrum of compound $[Fe^{II}(MeIm)_2(Pc^{2-})]\cdot 2C_6H_4Cl_2$ (**4**) in KBr pellets. KBr pellet for **4** was prepared in anaerobic conditions.

Crystal structure of complex 1.

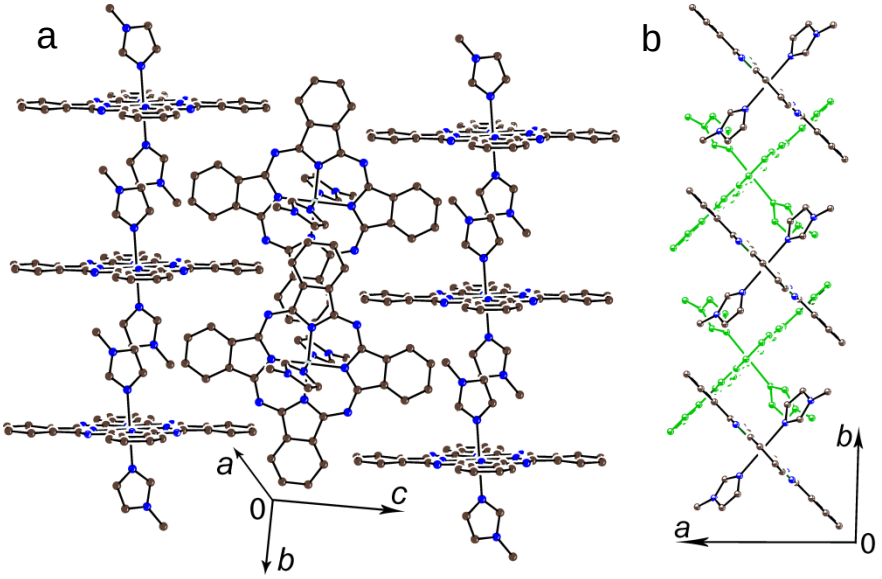

Fig. S5. Crystal structure of $[V^{II}(MeIm)_2(Pc^{2-})]\cdot MeIm$ (**1**). View on perpendicular to the Pc macrocycles of one of the chains in **1** (a) and view on two such chains along the *c* axis (b). In the latter case the $[V^{II}(MeIm)_2(Pc^{2-})]$ molecules from the behind located chain are shown by green color.

Magnetic properties of compounds 1–3.

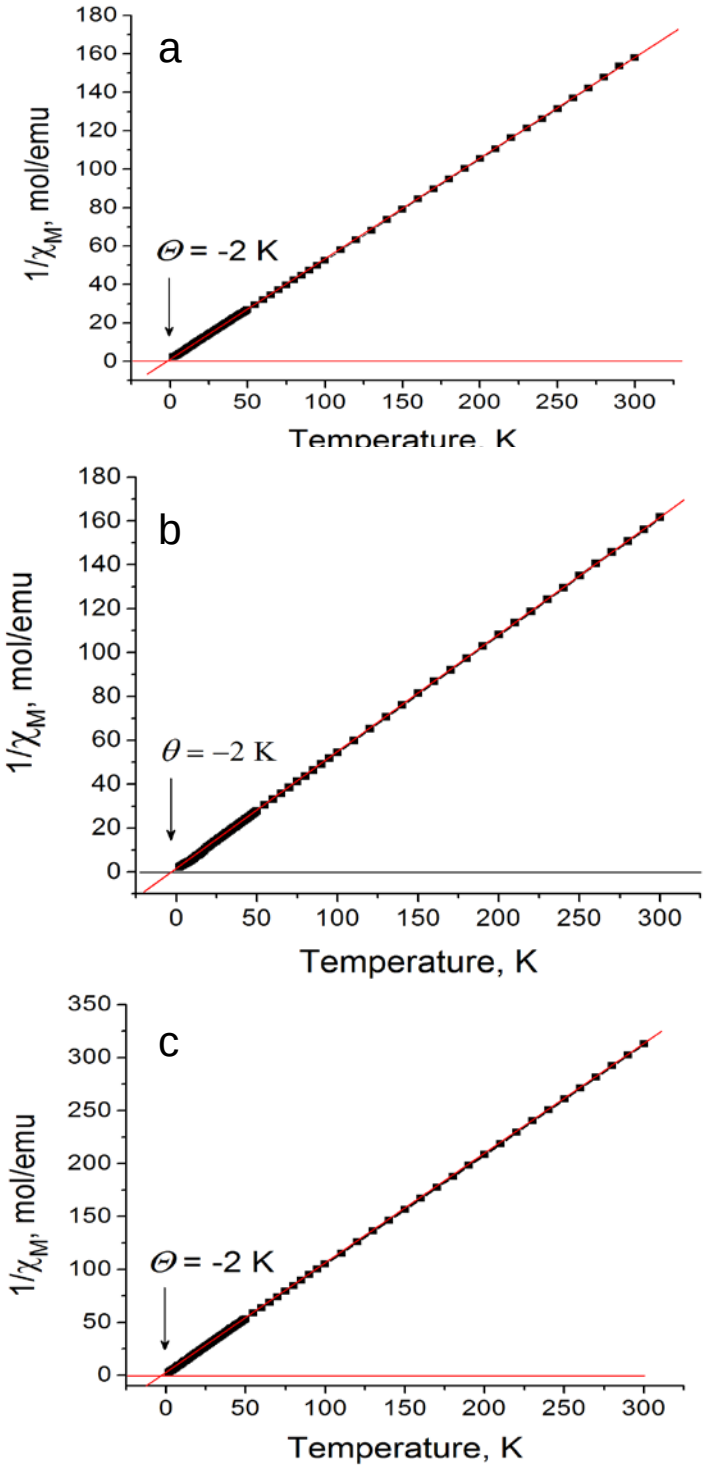

Fig. S6. Temperature dependencies of resiprocal molar magnetic sysceptibilities for the complexes: (a) $[V^{II}(MeIm)_2(Pc^{2-})]\cdot MeIm$ (**1**); (b) $[V^{II}(MeIm)_2(Pc^{2-})]\cdot 2C_6H_4Cl_2$ (**2**) and (c) $[Cr^{II}(MeIm)_2(Pc^{2-})]\cdot 2C_6H_4Cl_2$ (**3**). Fitting of the data by the Curie-Weiss law shown by red line allows to determine Weiss temperature ($\Theta = -2$ K for **1**–**3**).

Table S2. Total and relative energies (E and ΔE), and $\langle S^2 \rangle$ values of $[V(MeIm)_2Pc]^0$ and $[Cr(MeIm)_2Pc]^0$ complexes calculated at the CAM-B3LYP/cc-pVTZ/cc-pVDZ level of theory

State	E / hartree	ΔE / K	$\langle S^2 \rangle$
$[V(MeIm)_2Pc]^0$			
^4A_g	−3141.43500	0	3.790
^2A_g	−3141.42704	2511	1.835
$[Cr(MeIm)_2Pc]^0$			
^5A_g	−3241.90947	3277	6.060
^3A_g	−3241.91984	0	2.871
^1A_g	−3241.88647	10540	1.767

Table S3. Charge and spin densities of the ^{4}Ag state in $[V(MeIm)_2Pc]^0$ and the ^{3}Ag state in $[Cr(MeIm)_2Pc]^0$ calculated at the CAM-B3LYP/cc-pVTZ/cc-pVDZ level of theory

	MPA		NPA		
	Charge	Spin	Charge	Spin	Natural electron configuration
$[V(MeIm)_2Pc]^0$					
V	0.597	2.460	0.838	2.262	$3d^{2.74}$
Pc	−1.211	0.534	−1.358	0.675	
MeIm	0.307	0.003	0.260	0.031	
$[Cr(MeIm)_2Pc]^0$					
Cr	0.682	2.921	0.792	2.699	$3d^{4.23}$
Pc	−1.336	−0.897	−1.429	−0.739	
MeIm	0.327	−0.012	0.318	0.020	

Table S4. Occupation numbers of natural orbitals, n(HO−1), n(HO), n(SO−1), n(SO), n(SO+1), n(LU), and n(LU+1), non-spin-projected and spin-projected diradical characters, y_i and y_i^{SP} (i = 0 and 1)[a,b], of the ^4A_g state in $[V(MeIm)_2Pc]^0$, the ^3A_g state in $[Cr(MeIm)_2Pc]^0$, and open-shell singlet states in acenes at the CAM-B3LYP/cc-pVTZ/cc-pVDZ level of theory

	$[V(MeIm)_2Pc]^0$	$[Cr(MeIm)_2Pc]^0$	Pentacene	Hexacene	Heptacene	Octacene
n(LU+1)	0.005	0.012	0.014	0.055	0.097	0.147
n(LU)	0.007	0.579	0.118	0.407	0.589	0.708
n(SO+1)	1.000	1.000	–	–	–	–
n(SO)	1.000	–	–	–	–	–
n(SO+1)	1.000	1.000	–	–	–	–
n(HO)	1.993	1.421	1.882	1.593	1.411	1.292
n(HO−1)	1.995	1.988	1.986	1.945	1.903	1.853
y_0	0.007	0.579	0.118	0.407	0.589	0.708
y_1	0.005	0.012	0.014	0.055	0.097	0.147
y_0^{SP}	0.000	0.285	0.008	0.123	0.296	0.462
y_1^{SP}	0.000	0.000	0.000	0.002	0.005	0.012

[a] $y_i = n(\mathrm{LU}+i) = 2 - n(\mathrm{HO}-i)$. [b] $y_i^{SP} = n^{SP}(\mathrm{LU}+i) = 2 - n^{SP}(\mathrm{HO}-i) = [n(\mathrm{LU}+i)]^2/(1 + S_i^2) = 2 - [n(\mathrm{HO}-i)]^2/(1 + S_i^2)$, $S_i = [n(\mathrm{HO}-i) - n(\mathrm{LU}+i)]/2$.

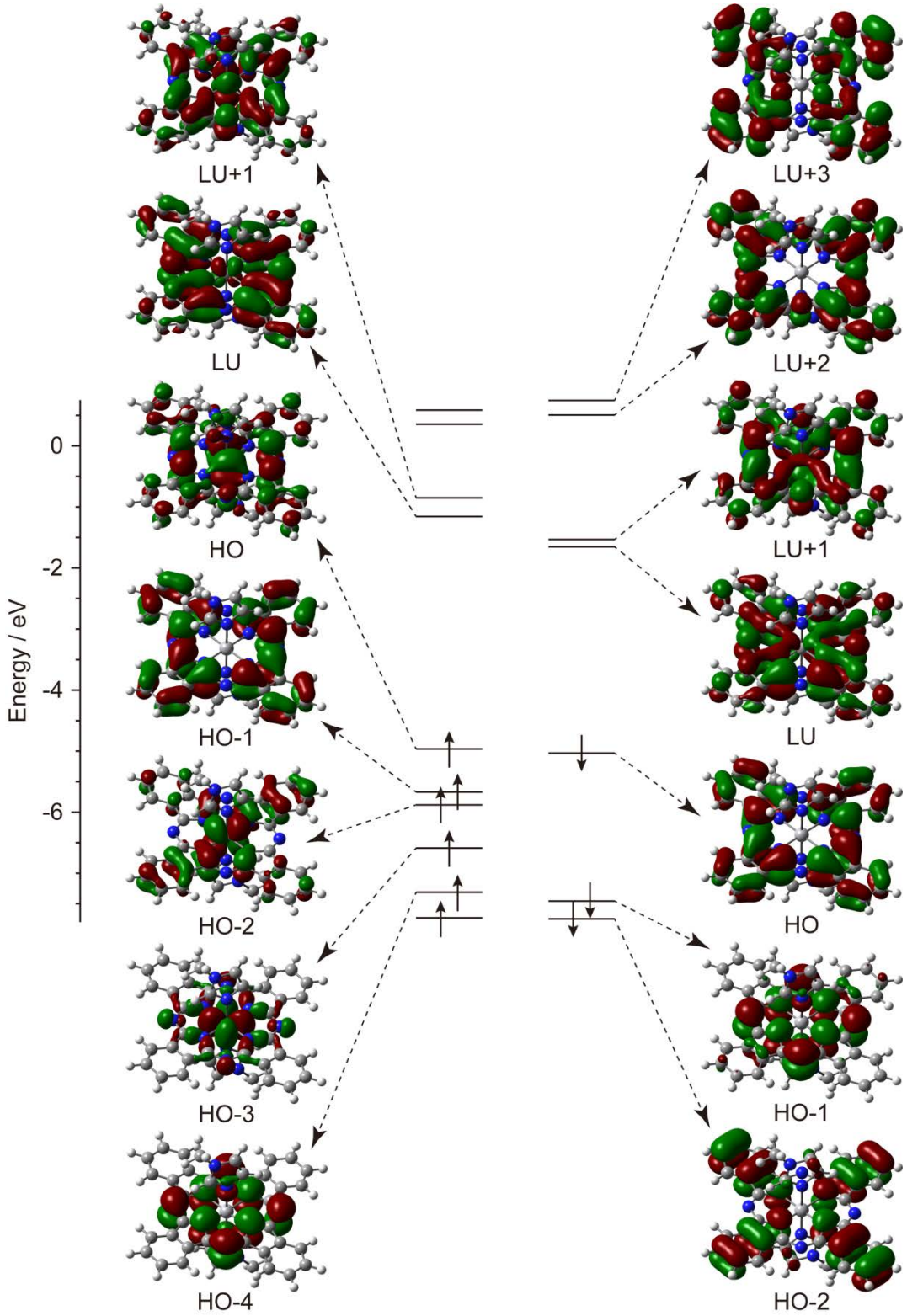

Fig. S7. Energy diagram for the frontier Kohn-Sham orbitals of the ^4A_g state in $[V(MeIm)_2Pc]^0$ calculated at the UCAM-B3LYP/cc-pVTZ/cc-pVDZ level of theory. HO and LU denote the highest occupied and the lowest unoccupied orbitals, respectively.

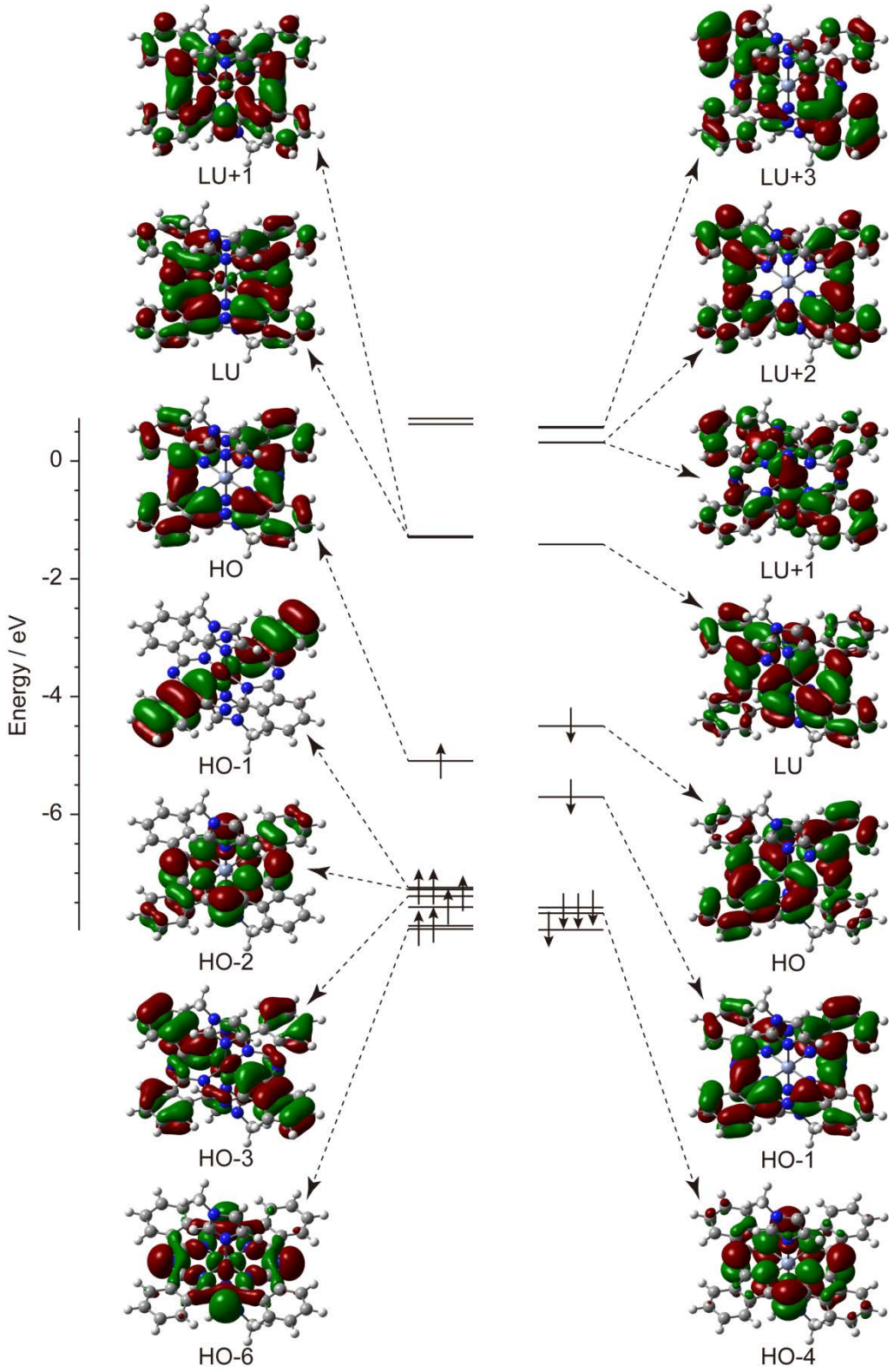

Fig. S8. Energy diagram for the frontier Kohn-Sham orbitals of the ^3A_g state in $[Cr(MeIm)_2Pc]^0$ calculated at the UCAM-B3LYP/cc-pVTZ/cc-pVDZ level of theory. HO and LU denote the highest occupied and the lowest unoccupied orbitals, respectively.

Table S5. Excitation energies (ΔE), oscillator strengths (f), $\langle S^2 \rangle$ values and assignments on the low-lying excited states of $[V(MeIm)_2Pc]^0$ calculated at the TD-UCAM-B3LYP/cc-pVTZ/cc-pVDZ level of theory.

	ΔE / eV	ΔE / nm	f	$\langle S^2 \rangle$	Assignment
1	0.655	1893	0.000	3.818	189α → 190α: 60% (α-HO → α-LU) 187α → 191α: 20% (α-HO-2 → α-LU+1) 189α → 191α: 9% (α-HO → α-LU+1) 187α → 190α: 4% (α-HO-2 → α-LU)
2	0.696	1782	0.031	5.150	186β → 187β: 80% (β-HO → β-LU) 188α → 190α: 14% (α-HO-1 → α-LU)
3	0.768	1616	0.000	3.818	189α → 191α: 60% (α-HO → α-LU+1) 187α → 190α: 24% (α-HO-2 → α-LU) 189α → 190α: 10% (α-HO → α-LU) 187α → 191α: 5% (α-HO-2 → α-LU+1)
4	0.842	1473	0.000	3.797	187α → 191α: 64% (α-HO-2 → α-LU+1) 189α → 190α: 27% (α-HO → α-LU) 178α → 191α: 3% (α-HO-11→ α-LU+1)
5	1.030	1204	0.068	4.485	186β → 188β: 86% (β-HO → β-LU+1) 188α → 191α: 7% (α-HO-1 → α-LU+1)
6	1.204	1030	0.000	3.788	186α → 191α: 88% (α-HO-3 → α-LU+1) 186α → 196α: 3% (α-HO-3 → α-LU+6) 175α → 191α: 3% (α-HO-14 → α-LU+1)
7	2.106	589	0.000	3.832	186α → 190α: 91% (α-HO-3 → α-LU) 187α → 190α: 3% (α-HO-2 → α-LU)
8	2.262	548	0.000	3.898	187α → 190α: 66% (α-HO-2 → α-LU) 189α → 191α: 25% (α-HO → α-LU+1) 186α → 190α: 4% (α-HO-3 → α-LU)
9	2.356	526	0.419	4.151	188α → 190α: 75% (α-HO-1 → α-LU) 186β → 187β: 15% (β-HO → β-LU) 185α → 191α: 4% (α-HO-4 → α-LU+1)
10	2.473	501	0.199	4.521	188α → 191α: 81% (α-HO-1 → α-LU+1) 186β → 188β: 7% (β-HO → β-LU+1) 185α → 190α: 6% (α-HO-4 → α-LU)
11	2.805	442	0.004	4.871	189α → 192α: 31% (α-HO → α-LU+2) 185β → 188β: 15% (β-HO-1 → β-LU+1) 185β → 187β: 10% (β-HO-1 → β-LU) 185α → 191α: 7% (α-HO-4 → α-LU+1) 185α → 190α: 6% (α-HO-4 → α-LU) 184α → 190α: 4% (α-HO-5 → α-LU) 184β → 187β: 4% (β-HO-2 → β-LU)

Table S5. (Continued)

	ΔE / eV	ΔE / nm	f	$\langle S^2 \rangle$	Assignment
12	2.835	437	0.000	3.788	187α → 209α: 55% (α-HO-2 → α-LU+19) 187α → 219α: 9% (α-HO-2 → α-LU+29) 187α → 207α: 7% (α-HO-2 → α-LU+17) 178α → 209α: 6% (α-HO-11 → α-LU+19) 187α → 221α: 4% (α-HO-2 → α-LU+31) 187α → 199α: 3% (α-HO-2 → α-LU+9) 187α → 212α: 3% (α-HO-2 → α-LU+22)
13	2.880	431	0.001	5.239	185β → 187β: 51% (β-HO-1 → β-LU) 185α → 190α: 21% (α-HO-4 → α-LU) 185β → 188β: 5% (β-HO-1 → β-LU+1) 189α → 192α: 4% (α-HO → α-LU+2) 185α → 191α: 4% (α-HO-4 → α-LU+1)
14	3.057	406	0.054	4.906	189α → 193α: 28% (α-HO → α-LU+3) 184β → 188β: 6% (β-HO-2 → β-LU+1) 186β → 191β: 6% (β-HO → β-LU+4) 182β → 187β: 6% (β-HO-4 → β-LU) 187α → 192α: 6% (α-HO-2 → α-LU+2) 188α → 196α: 5% (α-HO-1 → α-LU+6) 184α → 191α: 3% (α-HO-5 → α-LU+1) 183α → 190α: 3% (α-HO-6 → α-LU)
15	3.088	401	0.004	5.018	185β → 188β: 36% (β-HO-1 → β-LU+1) 185α → 191α: 18% (α-HO-4 → α-LU+1) 182β → 188β: 6% (β-HO-4 → β-LU+1) 189α → 192α: 5% (α-HO → α-LU+2) 186β → 192β: 4% (β-HO → β-LU+5) 184β → 187β: 3% (β-HO-2 → β-LU)
16	3.113	398	0.000	5.353	186β → 190β: 17% (β-HO → β-LU+3) 188α → 193α: 10% (α-HO-1 → α-LU+3) 189α → 195α: 6% (α-HO → α-LU+5) 181β → 187β: 5% (β-HO-5 → β-LU) 186β → 189β: 5% (β-HO → β-LU+2) 180α → 195α: 4% (α-HO-9 → α-LU+5) 183β → 188β: 3% (β-HO-3 → β-LU+1) 186α → 209α: 3% (α-HO-3 → α-LU+19) 179β → 192β: 3% (β-HO-7 → β-LU+5)

Table S5. (Continued)

	ΔE / eV	ΔE / nm	f	$\langle S^2 \rangle$	Assignment
17	3.130	396	0.000	5.352	183β → 187β: 10% (β-HO-3 → β-LU) 189α → 195α: 6% (α-HO → α-LU+5) 186β → 189β: 5% (β-HO → β-LU+2) 186β → 193β: 5% (β-HO → α-LU+3) 182α → 190α: 5% (α-HO-7 → α-LU) 186β → 190β: 5% (β-HO → β-LU+3) 188α → 194α: 5% (α-HO-1 → α-LU+4) 183β → 188β: 4% (β-HO-3 → β-LU+1) 181α → 196α: 3% (α-HO-8 → α-LU+6) 184β → 189β: 3% (β-HO-2 → β-LU+2) 186α → 209α: 3% (α-HO-3 → α-LU+19) 184α → 192α: 3% (α-HO-5 → α-LU+2)
18	3.214	386	0.000	4.010	189α → 209α: 30% (α-HO → α-LU+19) 186α → 209α: 20% (α-HO-3 → α-LU+19) 189α → 219α: 5% (α-HO → α-LU+29) 189α → 207α: 4% (α-HO → α-LU+17) 186α → 219α: 4% (α-HO-3 → α-LU+29) 189α → 199α: 3% (α-HO → α-LU+9)
19	3.221	385	0.000	4.278	186α → 209α: 28% (α-HO-3 → α-LU+19) 189α → 209α: 13% (α-HO → α-LU+19) 186β → 189β: 12% (β-HO → β-LU+2) 186α → 219α: 5% (α-HO-3 → α-LU+29) 186α → 207α: 3% (α-HO-3 → α-LU+17) 188α → 192α: 3% (α-HO-1 → α-LU+2) 186β → 190β: 3% (β-HO → β-LU+3)
20	3.233	384	0.000	5.001	186β → 189β: 39% (β-HO → β-LU+2) 189α → 209α: 14% (α-HO → α-LU+19) 188α → 192α: 10% (α-HO-1 → α-LU+2) 180β → 187β: 4% (α-HO-9 → β-LU) 186α → 209α: 3% (α-HO-3 → α-LU+19)

Table S6. Excitation energies (ΔE), oscillator strengths (f), $\langle S^2 \rangle$ values and assignments on the low-lying excited states of $[Cr(MeIm)_2Pc]^0$ calculated at the TD-UCAM-B3LYP/cc-pVTZ/cc-pVDZ level of theory.

	ΔE / eV	ΔE / nm	f	$\langle S^2 \rangle$	Assignment
1	0.407	3048	0.000	2.924	187β → 188β: 96% (β-HO → β-LU)
2	1.012	1225	0.008	4.537	189α → 191α: 34% (α-HO → α-LU+1) 189α → 190α: 33% (α-HO → α-LU) 186β → 188β: 24% (β-HO-1 → β-LU) 187β → 191β: 4% (β-HO → β-LU+3)
3	1.460	849	0.129	3.087	189α → 190α: 48% (α-HO → α-LU) 189α → 191α: 45% (α-HO → α-LU+1) 187β → 190β: 4% (β-HO → β-LU+2)
4	2.253	550	0.000	2.533	187β → 189β: 84% (β-HO → β-LU+1) 187β → 197β: 4% (β-HO → β-LU+9) 187β → 195β: 3% (β-HO → β-LU+7)
5	2.301	539	0.394	2.960	186β → 188β: 62% (β-HO-1 → β-LU) 189α → 191α: 14% (α-HO → α-LU+1) 189α → 190α: 12% (α-HO → α-LU) 187α → 190α: 3% (α-HO-2 → α-LU)
6	2.376	522	0.000	2.099	187β → 193β: 94% (β-HO → β-LU+5)
7	2.431	510	0.000	2.716	187β → 192β: 83% (β-HO → β-LU+4) 187β → 198β: 3% (β-HO → β-LU+10)
8	2.444	507	0.214	3.688	187β → 190β: 59% (β-HO → β-LU+2) 187α → 191α: 10% (α-HO-2 → α-LU+1) 183β → 188β: 7% (β-HO-4 → β-LU) 187α → 190α: 7% (α-HO-2 → α-LU) 186β → 189β: 3% (β-HO-1 → β-LU+1)
9	2.832	438	0.000	2.988	174α → 197α: 31% (α-HO-15 → α-LU+7) 186α → 197α: 17% (α-HO-3 → α-LU+7) 188α → 197α: 15% (α-HO-1 → α-LU+7) 179α → 197α: 9% (α-HO-10 → α-LU+7) 163α → 197α: 8% (α-HO-26 → α-LU+7)
10	2.841	436	0.003	3.569	187β → 191β: 44% (β-HO → β-LU+3) 187β → 194β: 18% (β-HO → β-LU+6) 186β → 188β: 10% (β-HO-1 → β-LU) 186β → 192β: 6% (β-HO-1 → β-LU+4)
11	2.894	428	0.000	2.993	173α → 197α: 30% (α-HO-16 → α-LU+7) 186α → 197α: 19% (α-HO-3 → α-LU+7) 188α → 197α: 15% (α-HO-1 → α-LU+7) 168α → 197α: 13% (α-HO-21 → α-LU+7)

Table S6. (Continued)

	ΔE / eV	ΔE / nm	f	$\langle S^2 \rangle$	Assignment
12	2.938	422	0.000	3.976	188α → 190α: 12% (α-HO-1 → α-LU) 187β → 198β: 10% (β-HO → β-LU+10) 189α → 193α: 9% (α-HO → α-LU+3) 188α → 191α: 9% (α-HO-1 → α-LU+1) 186β → 191β: 8% (β-HO-1 → β-LU+3) 186β → 194β: 5% (β-HO-1 → β-LU+6) 189α → 195α: 5% (α-HO → α-LU+5) 187β → 195β: 4% (β-HO → β-LU+7) 187β → 197β: 4% (β-HO → β-LU+9) 186α → 191α: 3% (α-HO-3 → α-LU+1) 184α → 196α: 3% (α-HO-5 → α-LU+6) 186α → 190α: 3% (α-HO-3 → α-LU)
13	3.182	390	0.000	4.249	186α → 191α: 15% (α-HO-3 → α-LU+1) 186α → 190α: 12% (α-HO-3 → α-LU) 189α → 193α: 7% (α-HO → α-LU+3) 178β → 188β: 5% (β-HO-9 → β-LU) 180α → 194α: 4% (α-HO-9 → α-LU+4) 184α → 191α: 3% (α-HO-5 → α-LU+1) 188α → 190α: 3% (α-HO-1 → α-LU) 184α → 190α: 3% (α-HO-5 → α-LU) 181β → 190β: 3% (β-HO-6 → β-LU+2)
14	3.198	388	0.025	3.621	187β → 191β: 29% (β-HO → β-LU+3) 187α → 190α: 16% (α-HO-2 → α-LU) 187β → 194β: 15% (β-HO → β-LU+6) 186β → 192β: 4% (β-HO-1 → β-LU+4) 189α → 196α: 3% (α-HO → α-LU+6) 187α → 191α: 3% (α-HO-2 → α-LU+1)
15	3.221	385	0.093	4.460	187α → 191α: 21% (α-HO-2 → α-LU+1) 183β → 188β: 21% (β-HO-4 → β-LU) 187β → 190β: 7% (β-HO → β-LU+2) 187α → 190α: 7% (α-HO-2 → α-LU) 181β → 188β: 6% (β-HO-6 → β-LU) 186β → 189β: 4% (β-HO-1 → β-LU+1) 189α → 194α: 3% (α-HO → α-LU+4)
16	3.284	378	0.000	4.087	189α → 192α: 34% (α-HO → α-LU+2) 188α → 190α: 19% (α-HO-1 → α-LU) 186β → 190β: 13% (β-HO-1 → β-LU+2) 187β → 195β: 9% (β-HO → β-LU+7)

Table S6. (Continued)

	ΔE / eV	ΔE / nm	f	$\langle S^2 \rangle$	Assignment
17	3.313	374	0.000	3.224	188α → 191α: 33% (α-HO-1 → α-LU+1) 188α → 190α: 21% (α-HO-1 → α-LU) 187β → 198β: 10% (β-HO → β-LU+10) 187β → 197β: 6% (β-HO → β-LU+9) 186β → 194β: 5% (β-HO-1 → β-LU+6) 189α → 192α: 4% (α-HO → α-LU+2) 185α → 192α: 3% (α-HO-4 → α-LU+2)
18	3.381	367	0.152	4.296	187β → 190β: 20% (β-HO → β-LU+2) 183β → 188β: 8% (β-HO-4 → β-LU) 189α → 194α: 6% (α-HO → α-LU+4) 181β → 188β: 5% (β-HO-6 → β-LU) 180α → 193α: 5% (α-HO-9 → α-LU+3) 179β → 191β: 4% (β-HO-8 → β-LU+3) 182α → 190α: 4% (α-HO-7 → α-LU) 178β → 190β: 3% (β-HO-9 → β-LU+2) 181α → 191α: 3% (α-HO-8 → α-LU+1)
19	3.437	361	0.335	3.275	187α → 190α: 35% (α-HO-2 → α-LU) 187α → 191α: 25% (α-HO-2 → α-LU+1) 187β → 191β: 12% (β-HO → β-LU+3) 185α → 190α: 6% (α-HO-4 → α-LU) 185α → 191α: 4% (α-HO-4 → α-LU+1) 189α → 191α: 3% (α-HO → α-LU+1) 187β → 194β: 3% (β-HO → β-LU+6)
20	3.522	352	0.000	3.884	184β → 188β: 18% (β-HO-3 → β-LU) 188α → 191α: 16% (α-HO-1 → α-LU+1) 186α → 190α: 14% (α-HO-3 → α-LU) 189α → 192α: 12% (α-HO → α-LU+2) 188α → 190α: 12% (α-HO-1 → α-LU) 186α → 191α: 10% (α-HO-3 → α-LU+1)